Flow-through reactor experiments on basalt-(sea)water-CO_2 reactions at 90 °C and neutral pH. What happens to the basalt pore space under post-injection conditions?

D. Wolff-Boenisch[1,2,*] and I. M. Galeczka[2,3]

[1]Department of Applied Geology, Curtin University, GPO Box U1987, Perth, 6845 Western Australia, Australia. Domenik.Wolff-Boenisch@curtin.edu.au
[2]Institute of Earth Science, University of Iceland, Sturlugata 7, 101 Reykjavik, Iceland
[3]Icelandic Geosurvey, Grensasvegur 9, 101 Reykjavik, Iceland

Abstract

Recent publications on the successful mineralisation of carbon dioxide in basalts in Iceland and Washington State, USA, have shown that mineral storage can be a serious alternative to more mainstream geologic carbon storage efforts to lock away permanently carbon dioxide. In this study we look at the pore solution chemistry and mineralogy of basaltic glass and crystalline basalt under post-injection conditions, i.e. after rise of the pH via matrix dissolution and the first phase of carbonate formation. Experimental findings indicate that further precipitation of carbonates under more alkaline conditions is highly dependent on the availability of divalent cations. If the pore water is deficient in divalent cations, smectites and/or zeolites will dominate the secondary mineralogy of the pore space, depending on the basalt matrix. At low carbonate alkalinity no additional secondary carbonates are expected to form meaning the remaining pore space is lost to secondary silicates, irrespective of the basalt matrix. At high carbonate alkalinity, some of this limited storage volume may additionally be occupied by dawsonite -if the Na concentration in the percolating groundwater (brine) is high. Using synthetic seawater as a proxy for the groundwater composition and thus furnishing considerable amounts of divalent cations to the carbonated solution, results in massive precipitation of calcite, magnesite, and other Ca/Mg-carbonates under already moderate carbonate alkalinity. More efficient use of the basaltic storage volume can thus be attained by promoting formation of secondary carbonates compared to the inevitable formation of secondary silicate phases at higher pH. This can be done by ensuring that the pore water does not become depleted in divalent cations, even after carbonate formation. Using seawater as carbonating fluid or injection of CO_2 into the basaltic oceanic crust, where saline fluids percolate, can reach this goal. However, such an approach needs sophisticated reactive transport modelling to adjust CO_2 injection rates in order to avoid too rapid carbonate deposition and clogging of the pore space too close to the injection well.

1. Introduction

Two recent publications on the injection of dissolved CO_2 into Icelandic basalt (Matter et al., 2016) as well as of supercritical CO_2 into Columbia River basalt (McGrail et al., 2017) showed that mineralisation of CO_2 within an unexpectedly short time frame of ≤ 2 years is feasible. These

efforts culminate a decade of lab and field research activities into various aspects of water-basalt-CO_2 interaction (Gislason et al., 2014; Gislason and Oelkers, 2014; Matter et al., 2016; McGrail et al., 2017). Given the unbridled use of fossil fuels, carbon storage has been stipulated to play an important role in reducing carbon emissions to the atmosphere by various energy scenarios (IEA, 2015; IPCC, 2014). Based on these recent field findings, and given the large storage potential (Snæbjörnsdottir et al., 2014) and vast volumes of basalt on the Earth (e.g. large igneous provinces, oceanic islands and oceanic crust), carbon storage into basalts may help curb CO_2 emissions via *in-situ* carbon mineralisation. Many laboratory and modelling studies confirmed the field observations (or rather preceded them) by anticipating that rapid carbonate precipitation would occur (Aradóttir et al., 2012; Gysi and Stefansson, 2012a, b; Pham et al., 2012; Rosenbauer et al., 2012; Schaef et al., 2013). However, these studies were carried out at very favourable conditions not realised in the field, where porosity and permeability play crucial roles in the extent of water-rock interactions. For one, powdered basalt has orders of magnitude higher reactive surface area compared to the pore surface area in the actual rock formation (Saar and Manga, 1999). The same holds for the specific surface area implemented into the reaction path/reactive transport models which is routinely based on gas adsorption measurements, the so-called A_{BET} (Brunauer et al., 1938), and presents maximum values. Even if based on geometric considerations (so-called A_{geo}), the specific surface area may well overestimate the available reactive surface area as pore connectedness and preferential flow have not been considered (Aradóttir et al., 2012; Sonnenthal et al., 2005; Steefel et al., 2015). This allows for more basalt to dissolve to (a) increase the pH to reach carbonate saturation and (b) provide the divalent cations required for carbonatisation. Second, the temperatures of the lab studies which found carbonate precipitation were between 50-100 °C, again considerably higher than the aquifer temperature range of 20-33 °C for Carbfix (Alfredsson et al., 2013) and 36 °C for Wallula (McGrail et al., 2017). Only the pressure range of field injections (4.5 and 7.7 MPa, respectively) and lab studies (around 10 MPa) were similar to rule out any minor pressure effect on carbonate solubility. Wolff-Boenisch et al. (2011) used PHREEQC (Parkhurst and Appelo, 1999) to model an acidity titration using composite basalt as sole base to neutralise the carbonic acid of a CO_2-ladden injection solution. The buffer capacity of such a (pore water) solution would increase one to two orders of magnitude to a pH of 5.6 meaning that per kg of solution 75g of basalt needs to dissolve to reach this pH, which is at the lower pH spectrum to expect (iron-containing) carbonate formation. Snæbjörnsdottir et al. (2017a) did reactive transport modelling to explain the carbonate yield at the Carbfix site and reported that 64 and 106 g of crystalline and basaltic glass, respectively had to dissolve per kg of injection fluid to explain the solution chemistry in the monitoring well. So despite some overly optimistic and/or simplistic approach, experiments and models do indeed converge to explain the field observations. However, Snæbjörnsdottir et al. (2017a) also found that beside 400 metric tonnes of carbonates, another 585 tonnes of secondary silicates (460 tonnes zeolites and 125 tonnes smectites) precipitated in the Carbfix field trial. Their presence was expected from experiments, modelling and field observations but their contribution to the reduction of the effective basalt storage volume is considerable. Given the lower density range of zeolite (2.0-2.4 g/cm^3) and smectite group minerals (2.0-2.7 g/cm^3)

compared to carbonates (2.7-4.0 g/cm^3), at least 50% (closer to 80%) more matrix pore space was taken up by secondary silicates than by secondary carbonates at the Carbfix site. The Carbfix as well as Wallula field trials demonstrate that on a short interval injection carbonates form. The question remains what happens to the remaining pore volume after the first phase of carbon and silicate mineralisation; can it be further used for more, subsequent carbonate deposition or is it more likely to be filled with more secondary silicates?

To answer this question a set of flow-through reactor experiments was designed to look closer at carbonate vs. silicate formation in water-basalt-CO_2 systems relevant to post-CO_2 injection conditions, when the pH is high (neutral to slightly alkaline) and the divalent cation load low. In contrast to previous studies, CO_2 was not added as a separate phase (whether gaseous, liquid or supercritical) but in the form of ammonium bicarbonate (NH_4HCO_3). Rationale for this approach was (a) to mimic pore water conditions after post injection and during fluid migration through the basalt vesicles and pores, when much of the protons have been consumed and thus much of the CO_2(aq) converted into carbonate alkalinity and (b) to avoid CO_2 degassing after terminating the pressurised reactor experiments. Wolff-Boenisch et al. (2016) discussed the potential of carbonate precipitation ('flash scaling') that is impossible to control after degassing a pressurised batch experiment and that may have caused some of the carbonate precipitation described in the literature. The outcomes of this series of experiments, which also take the mineralogy and crystallinity of the basalt into account, are presented below.

2. Material&Method

2.1. Material

The basaltic glass and crystalline/compound basalt used in this study (referred to as 'G' and 'X' in figures and tables) were collected from the Stapafell Mountain in SW Iceland. The dissolution behaviour of the material under varying pH, T, organic ligand, saturation, and pCO_2 conditions has been previously described (Galeczka et al., 2014; Gislason and Oelkers, 2003; Gudbrandsson et al., 2011; Oelkers and Gislason, 2001; Stockmann et al., 2011; Wolff-Boenisch et al., 2011). The elemental composition of the basaltic glass is nearly identical to that of the crystalline basalt (Table 1). In contrast to the glass, the crystalline/compound basalt is a heterogeneous multi-phase solid consisting of 41 vol% labradoritic plagioclase, 34 vol% augitic clinopyroxene, 15 vol% forsteritic olivine and minor iron oxides and interstitial glass (Gudbrandsson et al., 2011). The material was crushed in a jaw crusher and dry sieved to obtain the particle size fraction of 45-100 (glass) and 45-125 (crystalline) µm which was subsequently washed by repeated gravitational settling to remove ultrafine particles. The resulting powder was dried at 50 °C for several days. The BET specific surface area of the cleaned powders was determined via 3-point krypton adsorption using a Quantachrome Gas Sorption system. Resulting BET surface areas equal 22,000 cm^2/g for the glass and 7030 cm^2/g for the crystalline basalt.

2.2. Method

The mixed-flow reactor system used for the experiments is illustrated in Figure 1. Two high pressure liquid chromatography (HPLC) pumps delivered the degassed inlet solution into two separate Parr™ titanium reactors. The fluid entered the bottom of the reactor via a dip tube. The 300 ml reactors were loaded with 7 g of powdered basaltic glass and crystalline basalt, respectively and heated up to 90 °C. The fluid/solid suspension was stirred constantly by a magnetic stirrer at approximately 90 rpm. To the outlet tubing of each reactor, a cooling sleeve was attached to cool the fluid down and facilitate fluid sampling and pH measurements at the outlet. Back pressure regulators (BPR) connected to both reactors were set at a minimum of 6 bars to keep the system pressurised. Samples were filtered twice; once when exiting the reactor through a 2 µm titanium filter and a second time at the outflow of the BPR, with a 0.2 µm acetate filter. Samples were acidified with 0.5 vol% concentrated suprapure HNO_3. The reactors were operated for 40 hours before the first sample was collected. The flow rates for both reactors were similar and adjusted such that the residence time of the fluid in the reactor was 25 hours. This allowed for prolonged fluid-rock interaction in the reactor and gave the flow-through experiments a semi-batch like character.

Inlet solutions were comprised of ultrapure Millipore™ water and Merck/Sigma-Aldrich analytical grade NH_4HCO_3, NaCl, KCl, $MgCl_2$, and $CaCl_2$. The experiment consisted of three separate, non-sequential series, with the major changing parameter being the inlet solution chemistry. The experimental set-up, flow rates, total pressures and the solid material was kept the same.

2.3. Protocol

In the first series (G40/X40), an inlet solution of 40 m*m* (millimolal; mmol/kg_w) ammonium bicarbonate was pumped through each reactor at a constant flow rate of 0.2 ml/min. Based on charge balance and initial inlet solution composition, the in-situ reactor pH at the temperature of 90 °C and 6 bar was calculated with PHREEQC3 (Parkhurst and Appelo, 2013) to be ~7. This experiment mimics the situation where the pH of a carbonated injection fluid of low DIC (corresponding to 4 bar pCO_2) has been neutralised through (a combination of) dilution with the groundwater, sustained basaltic rock dissolution, and mobilisation of carbonates initially present in the formation, and where divalent cations have been incorporated into carbonates and secondary silicate phases, e.g. Ca-Fe smectites such as saponite and/or nontronite (Gysi and Stefansson, 2012a). It represents a later phase of CO_2 injection that has migrated further away from the injection well.

In the second series (G400/X400), a 400 m*m* ammonium bicarbonate solution was used as inlet solution thus increasing the DIC ten-fold to mimic an injection fluid of higher pCO_2 (40 bar). Again, the system was kept deliberately at cation depletion (i.e. no divalent cations were added with the ammonium bicarbonate) to see in how far the basalt itself can source the divalent cations required to reach carbonate saturation.

In the third series, a 440 m*m* ammonium bicarbonate solution was mixed with sulphate-free artificial seawater in a volume ratio of 2.5:1 (see Table 2 for flow rates) resulting in an ammonium bicarbonate concentration of 315 m*m* in the mixture. Further in the text this experiment will be referred to as 315 m*m* experiment. The seawater was prepared by NaCl, KCl, $MgCl_2$, and $CaCl_2$ salts according to ion concentrations found in Millero (2003). Sulphate was deliberately omitted from this 'seawater' experiment to avoid interference of anhydrite with the expected carbonate formation. This experiment was meant to mimic basaltic reservoir conditions under the ocean where the treated injection fluid migrates into saline pores of high ionic strength and rich in divalent cations but absence of sulphate. This third series focussed on the glass matrix alone (GSW). All experimental conditions have been tabulated in Table 2.

The Si, Na, Mg, Ca, Fe, and Al concentrations of all inlet and outlet fluids were measured by inductively coupled optical emission spectrometry (ICP-OES). Due to high salinity of the samples they were diluted up to six times. Analytical uncertainties of ICP-OES analyses were on the order of ≤5%. Solids before and after each experimental series were analysed using a LEO Supra 25 and a JEOL 6360 LV Scanning Electron Microscope. The solids were coated with carbon prior to the analysis that used an acceleration voltage of 15 kV. Energy Dispersive X-ray Spectroscopy (EDX) was used together with SEM to identify primary and secondary minerals. Selected samples were analysed by X-ray diffraction (XRD) to confirm the identity of secondary minerals.

2.4. Geochemical Modelling

Modelling of the mineral saturation indices was carried out with PHREEQC3 (Parkhurst and Appelo, 2013) together with the *phreeqc.dat* database. It was modified with the aqueous complex formation and mineral solubility constants reported by Gysi and Stefansson (2011). The thermodynamic properties of NH_4-dawsonite were calculated based on Na-dawsonite, taken from the *llnl* database by replacing the Na for NH_4 in the hydrolysis reaction. All saturation calculations have been compiled in a supplementary material file, separated by experiment and grouped as carbonate versus silicate phases for better viewing.

3. Results

3.1. The 40 millimolal ammonium-bicarbonate experiment at 90°C with the glass (G40) and crystalline/compound basalt (X40), respectively.

Figure 2 summarises the evolution of pH and DIC for this first set. Due to proton consumption and dissolution reactions the pH rose in both basalt systems from 7 to 7.5 whereas the DIC remained plus/minus constant around 40 mm. Similar pH in both systems were expected because the dissolution rates of glass and olivine are similar under those conditions. Furthermore, the inlet solution has substantial buffering capacity to avoid larger pH increases. The concomitant solution chemistry is summarised in Fig. 3. The first 240h of the basaltic glass experiment and first 170 h of the crystalline basalt experiment were unusual because normally, under flow-through

conditions, initial solute concentrations are very high while sharp grain features such as edges are rounded and ultrafine particles dissolve. Over time, solute concentrations decrease and finally reach steady-state. Here, however, the first pulse raised the silica (and Ca/Mg) concentrations before they started their expected monotonical descent. Reason for this deviation may be found in the sampling interval which was 24 h, a little less than one mechanical mixing in the reactor (25 h, see table 2). Routinely, three residence times are observed to ensure thorough mechanical mixing before samples are taken (Oelkers and Gislason, 2001). Because the initial solution in which the particles were submersed was DI water saturated with atmospheric CO_2, the slow thorough initial mixing and displacement of DI water from the reactor may explain the unusual solute pulse of the first part of the experiment. The protocol of sampling after only one mechanical mixing interval seemed more practical and the shorter sampling time did not affect the outcome of this study which was not about finding representative steady-state dissolution rates or rate expressions, for which longer sampling intervals should be observed. After reaching a maximum, the silica concentration kept decreasing over time in both basalt systems, very slowly for the glass and more markedly for the crystalline basalt. This monotonical decent indicates the formation of secondary silicate phases increasing thus the available surface area over time onto which to grow. The major divalent cations Ca and Mg reached a comparable pseudo steady-state for the glass only towards the end of the experiment, while more Ca than Mg was released from the crystalline material. Na concentrations were low and constant and Al and Fe had largely been removed due to secondary mineral formations in both matrices. Because the silica concentration kept declining, stoichiometric considerations were based on Na, an element considered more conservative in comparison to other major elements of a rock matrix. Figure 4 displays that glass dissolution was close to stoichiometric only for Ca. This indicates that no Ca-bearing carbonates formed from the glass despite the system being supersaturated with calcite and dolomite for the first 250 h (see supplementary material). The mineral saturation calculations suggest that magnesite may have formed as the solution remains at magnesite saturation for nearly the entire experimental duration. However, no bubbles were observed when treating the reacted glass material with diluted hydrochloric acid. Because the iron concentrations in the outlet were so low, saturation indices of multiple iron-bearing carbonate phases were negative throughout the experimental duration (see supplementary material).

Evidently, no stoichiometry was observed for the compound basalt but the prevalence of aqueous Ca and plus/minus steady Ca/Na solute ratio (Fig. 4) again indicate the absence of Ca-bearing carbonates. To find out more about the secondary phases that precipitated in both systems, SEM coupled with EDX were carried out on the reacted material and compared to saturation index calculations.

The basaltic glass experiment G40 showed pervasive iron precipitates, easily observable on the reactor wall but also via SEM on the glass surface. This alteration product assumed either the shape of granular spheres (Fig. 5a) or was incorporated into of a thin veneer of a secondary silicate mineral (Fig. 5b-d). Trying to identify the major silica sink proved elusive. Figure 5b and

5c illustrate the representative alteration assemblage of the glass, with the pristine glass surface cropping up through an iron-rich silicate veneer. Matching EDX of that overgrowth with mineral formulae could equally well describe an Mg(-Fe) smectite or a Mg zeolite (e.g. chabazite) with the iron signal stemming from the underlying glass matrix. Saturation index calculations for these two mineral groups were all over the graph (see supplementary material) which is not too surprising given the wide range of possible solid solutions. Enlisting the help of XRD on the reacted glass did not clear this ambiguity as there was little crystalline material; however, the few peaks that went above the detection limit (2%) were more in line with a clay mineral of the smectite group than a zeolite. No other secondary phase was detected to pin down the quantitative removal of Al; saturation index calculations point to kaolinite and/or gibbsite as possible additional secondary Al phases as the solution was supersaturated with respect to both minerals in the beginning. Likewise, no carbonates were observed in the SEM-EDX, consistent with the diluted hydrochloric acid test.

The secondary mineralogy of X40 showed similarities and discrepancies to G40. Similarities included the absence of secondary carbonates, also confirmed by the lack of gas bubbles when treated with dilute hydrochloric acid, and the presence of a thin iron rich silicate layer covering the mineral surface. However, there was less iron in the mineral coatings and none on the reactor walls. This observation is consistent with the notion that the iron in the crystalline basalt is concentrated in a few mineral phases, mainly augite (34 vol%), iron oxide (5 vol%), and interstitial glass (4 vol%) and therefore not as homogeneously distributed and readily available as in the glass (note, the olivine is a forsterite and contains comparatively little iron). Major difference to the G40 experiment was the type and amount of silicate that precipitated. Figures 6a-c display the secondary silicate clusters that was commonly found on the reacted mineral surface and which was not observed in G40. At a closer look, these clusters grew on top of a mat that covered the original mineral surface (Fig. 6d). This epitaxial growth was very thin such that its EDX basically gave the composition of the underlying labradorite but it contained some iron. It appears to be of similar nature as the iron-rich silicate veneer described for G40 but the latter had a lot higher iron content. The clusters themselves contained similar atomic % of Al and Si on one hand and Na and Ca on the other and were best described as a zeolite-type mineral (Ca-Thomsonite), in accordance with field observations on the metasomatic alteration of compound basalts (Rogers et al., 2006). So the low ionic strength and DIC experimental set yielded secondary mineral assemblages that varied from the glassy to the crystalline basalt but are similar to literature observations under hydrothermal CO_2-rich weathering conditions.

3.2. The 400 millimolal ammonium-bicarbonate experiment at 90°C with the glass (G400) and crystalline/compound basalt (X400), respectively.

Keeping the inlet solution chemistry constant in this set proved more challenging than for the 40 m*m* set. Because of some degradation of the thermally labile NH_4HCO_3, the DIC of the inlet solution fluctuated somewhat whereas the outlet pH ranged between 8.3 and 8.5 (Fig. 7). Like in the previous glass dissolution experiment (G40), Ca and Mg dissolved at the same pace in the

G400 experiment; only towards the end of the experiment did the Ca concentration decline more strongly than for Mg (Fig. 8). The Na concentrations stayed low and constant and Fe and Al were incorporated into secondary precipitates, again similar to the G40 experiment. In contrast, in the compound basalt experiment (X400) Mg replaced Ca as the major solute cation compared to the X40 experiment. As for the other cations in the X400 experiment, Al and Fe concentrations were very low and consistent with incorporation into secondary phases, like in X40, but Na did not behave conservatively anymore. Its concentration declined steadily to near zero over the experimental duration, indicating formation of Na-bearing phases. Because the Na concentrations in G40 and G400 were similar and constant (0.02 m*m*), a stoichiometry plot of G400 based on Na was generated (Fig. 9). It indicates alternating conditions of minor secondary silicate deposition and stoichiometric Si and Mg release. In contrast, aqueous Ca/Na ratios were consistently lower indicating Ca loss from solution. Saturation index calculations suggest a potential sink to be calcite (see supplementary material) as the solution sat on saturation with respect to that carbonate phase throughout the entire experimental duration. Again, SEM-EDX was implemented to reveal potential precipitates that formed in this high ionic strength set.

The major secondary phase in G400 formed needles that either scattered randomly over entire glass fragments (Fig 10a) or came together in neat clusters (Fig. 10b). Application of diluted hydrochloric acid to the reacted glass suggested the presence of carbonates and EDX revealed the carbonate mineral to be a dawsonite-type carbonate, but with ammonium instead of Na, i.e. $NH_4AlCO_3(OH)_2$ (Lodziana et al., 2011). The solution was considerably supersaturated with dawsonite (see supplementary material) so that this finding may seem unsurprising but so was the G40 solution and no dawsonite had formed in that experiment. Iron was removed via iron pellets (Fig. 10c), whereas the intermittent sink for silica could not be determined. The surface coatings that were observed (Fig. 10d) were too thin to yield an EDX spectrum sufficiently separate from the underling glass but it is plausible to assume similar Fe-Mg smectites as inferred from the G40 experiment. So whereas there are observations and circumstantial evidence to suggest that Mg, Si, Fe and Al ended up in similar phases as in G40, the main difference to G40 is the appearance of NH_4-dawsonite. Note that of the eight EDX spectra that were taken from different needle assortments not a single one showed Na in the spectrum, thus corroborating its conservative status, as in G40. The fact that similar secondary phases were observed in G40 and G400, respectively (apart from the carbonate) is not surprising because only the nitrogen and carbon content had changed from G40 to G400 (and with it the ionic strength), whereas P and T had been kept constant and the pH gone up only marginally. Therefore, mineral saturation calculations of potential secondary silicate/oxide phases were similar in both glass experiments (see supplementary material).

Similarly, in the crystalline basalt experiment X400, NH_4-dawsonite also formed but to a lesser extent than in G400, as seen in less abundant needles in SEM (Figs. 11a-c) and the fact that the reacted compound basalt hardly responded to HCl treatment. As such, saturation indices (see supplementary material) that displayed the same degree of dawsonite supersaturation for both

inlet solutions, G400 and X400, are a poor measure of the likelihood of finding the phase precipitating out of solution.

Furthermore, iron precipitations did not form bright pellets like in G400 but were tied together like rosettes (Fig. 11b). A silicate phase, whose composition could not be ascribed unambiguously to a specific mineral group but whose appearance is similar to the needle clusters in Figures 6a-c, was found scattered over many of the different mineral surfaces (Figs. 11c-d). These observations suggest that similar phases formed for X40 and X400 (for similar reasons cited before for G40 vs. G400), with the major difference being dawsonite's appearance in X400.

3.3. The 315 millimolal ammonium bicarbonate - seawater experiment at 90°C with the glass (GSW).

This experiment was terminated prematurely after 111 hours because widespread white precipitation clogged the inlet of the reactor such that no fluid could flow in anymore. During that time only three samples had been taken suggesting considerable consumption of DIC within the reactor. The initial DIC after mixing with seawater was 315 m*m* whereas the DIC that was determined at the outlet (after the backpressure regulator) decreased, first to 87 and then to 33 m*m* at the termination of the experiment (Fig. 12). The solution chemistry also corroborated the formation of carbonates. In accord with saturation calculations derived from the inlet mix, the fluid had been supersaturated with an array of different carbonates and maintained supersaturation for the limited duration of the experiment (see supplementary material). Likewise, the divalent cation concentrations dropped significantly in the outlet (Fig. 13), a further sign of massive carbonate deposition. Unsurprisingly, inside the reactor, white precipitate appeared everywhere, from the reactor wall to the inner parts (propeller, inflow tubing). A first cursory check with HCl was positive so the precipitate was collected, dissolved in acid, diluted and analysed with ICP-OES. It turned out to be $CaCO_3$ with 9 mol% Mg. Apart from calcite, which was subsequently identified by its rhombohedral appearance via SEM (Fig. 14a-c), SEM-EDX also detected the presence of an amorphous looking Ca-carbonate (Fig. 14d) and a rhombohedral Mg-carbonate (Fig. 14e). The latter also showed rhombohedral appearance, like calcite, and is thus believed to be magnesite which has the same trigonal crystallographic structure as calcite. Furthermore, a secondary silicate, resembling strongly flaky chlorite, was observed; its EDX could be matched with chamosite.

4. Discussion

4.1. The 40 millimolal ammonium-bicarbonate experiment at 90°C with the glass (G40) and crystalline/compound basalt (X40), respectively.

In the absence of added divalent cations to the working solution, the G/X-40 mixed-flow reactor experiments did not yield any noticeable secondary carbonates during the 25 h of reaction/residence time. This was despite the solutions being supersaturated with respect to NH_4-dawsonite, magnesite, dolomite, and calcite for the first 250 h, that is, ten residence times, of the

experiment. Dawsonite remained supersaturated with respect to the outlet solutions throughout the experiment, but supersaturation declined with experimental time. Magnesite remained at saturation after 250 h until the end of the experiment (see supplementary material). Hence, it cannot be entirely ruled out that a small amount of NH_4- and Mg-carbonates precipitated, but it must have been precious little to evade HCl testing and SEM scrutiny. However, neither the DIC (Fig. 2) nor the Ca concentration (Fig. 4) are consistent with (Ca) carbonate formation. Instead, the secondary phases that formed in the G40 experiment were abundant iron oxides and very likely smectite type minerals. The presence of smectites rather than carbonates matches the findings of Hellevang et al. (2017) who also dissolved basaltic glass under similar pH-T conditions (pH 7.9, 80°C) but in batch mode. The authors reported the formation of smectites (nontronite) covering the entire surface of the basaltic glass (very much like in Figs. 5c,d) and the absence of carbonate crystals in the SEM. What makes this reference particularly applicable here is the fact that their inlet solution (at 80°C) was also void of any divalent cations which were only provided by the basaltic glass itself. Although their batch solution had become supersaturated with respect to secondary carbonates over the experimental duration of 26 days (SI of 1.9, 0.8, and 1.0 for dolomite, magnesite, and calcite, respectively) these phases did not form. As such, the relatively short residence time of 25 h in our flow-through experiments, despite being similarly supersaturated with carbonates, cannot be the reason to explain the absence of carbonates in our study. Hellevang et al. (2017) suggested inhibition of carbonate nucleation on smectite coated basalt grains and/or overestimated carbonate growth kinetics as most likely cause for the absence of carbonates. Gysi and Stefansson (2012b) also studied the hydrothermal alteration of basaltic glass under CO_2–rich conditions (at 75°C) and also reported thin silicate coatings on their altered basaltic glass surface, like the one in Fig. 5d, which they ascribed to Mg-Fe smectites. This reference also found secondary carbonates; however, their experimental set-up started with basalt-CO_2 interactions under acidic conditions in batch mode that lasted for 124 days which gave the system time to dissolve enough basalt and accumulate sufficiently large amounts of divalent cations in solution to precipitate Mg,Fe-carbonates.

As for other secondary non-silicate/carbonate phases, EDX cannot distinguish between any iron phase like iron hydroxide, goethite, ferrihydrite, or hematite. Gysi and Stefansson (2012b) found amorphous goethite in their basaltic glass alteration experiments at 75°C which corresponds well with saturation calculations for the G40 experiments where the fluid was slightly supersaturated with amorphous goethite over the entire experimental duration (see supplementary material).

Precipitations in the X40 experiment differed from G40 in that it yielded (a) visibly considerably less iron oxide phases and (b) more secondary silicates (also from a zeolite type) as indicated by the stronger degree of Si/Na non-stoichiometry (Fig. 4). This deviation in the secondary mineralogy is not surprising because the basaltic glass is a one-phase system that dissolves congruently whereas the crystalline basalt is a compound matrix of different mineral phases, all with their specific temperature and solution dependent dissolution rates (Gudbrandsson et al., 2011).

The X40 experiments compared favourably with the findings from Gudbrandsson et al. (2011) as the reference reported somewhat lower silica-based dissolution rates for the compound basalt at 75 °C and pH 7 compared to the glass. This trend was corroborated in this study in the silica concentration (open squares in Fig. 3) that reached a higher maximum derived from the glass compared to the crystalline basalt. Likewise, the Ca solute concentration in the compound basalt experiment was higher than the Mg solute concentration, again in accord with Gudbrandsson et al. (2011) who established preferential Ca release (over Mg and Fe) under neutral to alkaline pH conditions.

4.2. The 400 millimolal ammonium-bicarbonate experiment at 90°C with the glass (G400) and crystalline/compound basalt (X400), respectively.

In the G400/X400 set, carbonates did form in abundance but not the ones that would be expected from the literature (Gysi and Stefansson, 2012a, b; Hellevang et al., 2017; Pham et al., 2012; Rosenbauer et al., 2012); instead ammonium bearing dawsonite ($NH_4AlCO_3(OH)_2$) precipitated. The dawsonite is the product of high experimental ammonium concentrations and not expected to form under CO_2 injections in the field. Ammonium will certainly not be present in such quantities in a basaltic reservoir to force its incorporation into a carbonate phase but NaCl-rich brine intrusions into or advections through continental basalt (Fouillac et al., 1989) may provide sufficiently large Na concentrations to replace the ammonium and still form a Na bearing dawsonite, in the presence of sufficient amounts of bicarbonate and deficiency in divalent cations. This is the first time that dawsonite formation is reported under experimental conditions in a basaltic matrix which warrants a discussion on its likely occurrence in the field, especially because it has been considered a potential phase to mineralise CO_2 in saline aquifers rich in aluminosilicates (e.g. feldspars and muscovite) that are lacking divalent cations (Bénézeth et al., 2007; Hellevang et al., 2011; Kaszuba et al., 2011; Labus and Bujok, 2011; Worden, 2006). Especially strong indications for dawsonite formation under CO_2 injection conditions come from modelling studies (Knauss et al., 2005; Mohd Amin et al., 2014; Pham et al., 2011; Xu et al., 2004; Xu et al., 2007; Xu et al., 2010; Zerai et al., 2006) whereas corresponding lab experiments (Hangx and Spiers, 2009; Kaszuba et al., 2005) do not report dawsonite formation. This discrepancy can be explained by inaccurate/insufficient thermodynamic data on dawsonite (Kaszuba et al., 2011) but field studies also corroborate the dawsonite conundrum by either observing no or only minor dawsonite formation on one hand (Tambach et al., 2015; Wilkinson et al., 2009) or abundant dawsonite formation on the other hand (Baker et al., 1995; Gao et al., 2009; Golab et al., 2006; Worden, 2006). An explanation to this controversy was provided by Hellevang et al. (2011) who investigated the thermodynamic stability of dawsonite. According to the authors, dawsonite may well form in a saline aquifer in the presence of abundant solute Na and Al and high(er) initial pCO_2 conditions (i.e. under CO_2 injection conditions). In addition, studies performed by Hellevang et al. (2014) reveal that dawsonite forms only at temperatures from 80 °C to 120 °C. With decreasing CO_2 pressure over time, dawsonite will become unstable and dissolve, leading mainly to the precipitation of secondary kaolinite. The authors concluded

that dawsonite can only mineralise CO_2 in systems of continuously high CO_2 pressures, an inference that explains well why dawsonite was absent in our G/X40 experiments even though the solution was supersaturated with respect to dawsonite over the entire experimental duration. This assessment is in agreement with field observations from Moore et al. (2005) who described the co-existence of secondary dawsonite and kaolinite in a gas reservoir high in natural CO_2. The authors concluded that dawsonite precipitation occurred under high pCO_2 and that kaolinite deposition was subsequent, under declining pCO_2 conditions. Based on these field as well as thermodynamic findings, it stands to reason that even under very auspicious conditions, that is, high CO_2 pressure injection into a brine-like, NaCl-rich basaltic aquifer, any potential dawsonite deposition, as insinuated by our G400/X400 experiments, would over time lead to the remobilisation of the dawsonite. It is speculative to think what would happen to the remobilised CO_2, also because of the changes to the porosity/permeability of the basaltic matrix but because basalt is intrinsically rich in divalent cations, there is a likelihood that the CO_2 may not disperse or even diffuse out of the system but remain in the pores and become scavenged in other more stable secondary carbonates over time. This question will be taken up again in the discussion on the basaltic glass – seawater experiment (GSW) where not only high Na solute concentrations were present but also moderate amounts of Mg and Ca that competed with Na for incorporation into carbonates.

The crystalline basalt exhibited a high and sustained Mg solute concentration (Fig. 8) which is puzzling. The rationale for expecting more aqueous Ca than Mg is the fact that the primary Ca-bearing mineral, labradoritic plagioclase, displays higher dissolution rates at higher pH than olivine and augite. Gudbrandsson et al. (2011) demonstrated how the ratio of element release rates, $r_{Ca}/(r_{Ca}+r_{Mg}+r_{Fe})$, increased with increasing pH for the compound basalt. Because the silica solute concentration followed the same pattern as that of Mg in Fig. 8, the Mg solute prevalence is very likely related to forsterite dissolution, rather than quartz and magnesite (re)mobilisation. Forsterite saturation calculations indicate that this phase was highly undersaturated whereas anorthite was supersaturated during the entire experiment. It follows that forsterite still dissolved according to its far-from-equilibrium rate whereas plagioclase dissolution, under far-from-equilibrium conditions similar to that of forsterite at neutral pH, may have shown a saturation effect that slowed down the release of Ca. Such an explanation invoking a thermodynamic effect is also consistent with the observation that Mg was not the predominant cation from the experimental onset. In the beginning, Mg and Ca release rates were similar. The unexpected solute predominance of Mg cannot be explained by the 10-fold increase in the ionic strength of the NH_4HCO_3 inlet solution that distinguished X400 from X40. Pokrovsky and Schott (2000) studied the effect of ionic strength and pH on the dissolution of forsterite, which is the prime Mg carrier in the crystalline basalt along with augite. The authors did not find any effect of ionic strength on forsterite dissolution rates over the entire pH range. However, aqueous carbonate ions did *inhibit* forsterite dissolution under alkaline conditions. Given that X400 had roughly one order of magnitude higher carbonate activity than X40, it means that the Mg release from forsterite in X400 should have been around half an order of magnitude *lower* than in X40,

making the observed Mg solute predominance in X400 incompatible with the argument of a positive ion effect. It is important to keep in mind that the powdered crystalline basalt consists of different fragments of different phases. It means that any interpretation of the Mg solute signal deduced from the pure mineral phase forsterite may be either reinforced or weakened because the reactive surface area of the phase forsterite that is in contact with the fluid is unknown. As such, its contribution to the fluid chemistry is open to speculations.

4.3. The 315 millimolal ammonium bicarbonate - seawater experiment at 90°C with the glass (GSW).

Once divalent cations were added to the inlet solution in the form of artificial seawater deprived of sulphate, precipitation of Ca and to a lesser extent Mg carbonates was massive and widespread. This observation agrees well with thermodynamic modelling (Gysi and Stefansson, 2011, 2012a, b; Pham et al., 2012; Rosenbauer et al., 2012) as well as the field studies (Matter et al., 2016; McGrail et al., 2017; Snæbjörnsdottir et al., 2017a; Snæbjörnsdottir et al., 2017b) that demonstrated the formation of carbonates. After all, matrix dissolution starts right after CO_2 injection when the solution is still acidic and provides ample time not only to accumulate the crucial divalent cations in the pore space but also to raise the pH to carbonate supersaturation. Note, however, that no NH_4-dawsonite was detected by EDX, despite it being supersaturated at least three orders of magnitude more strongly than other carbonates such as dolomite, magnesite or calcite during the entire experiment (see supplementary material). Note also that the NH_4-dawsonite supersaturation in the GSW experiment was also a 1000-fold larger than in G400 that showed the largest degree of dawsonite formation. Assuming similar thermodynamic properties for NH_4-dawsonite and Na-dawsonite (Lodziana et al., 2011), it follows by extension that Na-dawsonite formation after CO_2 injection into a basaltic aquifer brine rich in NaCl is unlikely as long as there are also abundant divalent cations present to favour Ca/Mg carbonate deposition. Because this pre-requisite is usually met (Baker et al., 1991; You et al., 2003), there is no need to discuss the potential for remobilisation of this phase after pCO_2 decline over time as its appearance in the first place in a basaltic matrix is not favourable. The observation of dawsonite formation in G400 is still educating; all the more because it was absent in GSW, despite the latter displaying dawsonite SI three orders of magnitude higher. This may be related to the cation to carbonate ratio in solution. The importance of the solution stoichiometry, i.e. achievement of a ratio close to one between metal cation and carbonate anion for mono-mineralic carbonate growth has been investigated in multiple studies (Chhim et al., 2017; Hong and Teng, 2014; Larsen et al., 2010; Nehrke et al., 2007; Perdikouri et al., 2009; Zuddas and Mucci, 1994). Hellevang et al. (2017) proposed that (strong) deviation from stoichiometry might have been behind the absence of carbonates in some of their supersaturated experiments that only yielded smectites. To follow up on this possibility, the stoichiometric ratios of Ca/CO_3, Mg/CO_3, and NH_4/CO_3 of the short GSW experiment were determined. They are 0.68, 0.13, and 0.07, respectively for the two data points at 39 and 87 h, where the carbonate activity was constant (Fig, 12). As such, there were indeed more favourable Ca and Mg to carbonate ratios in solution which could explain why Ca

and Mg carbonates were observed in the SEM whereas dawsonite was absent. Likewise, the stoichiometric ratios of Ca/CO_3, Mg/CO_3, and NH_4/CO_3 were $2.2 \cdot 10^{-2}$, $8.2 \cdot 10^{-5}$, and 9.4 in the G400 experiment. The closer stoichiometry for NH_4 is again consistent with the observation of finding dawsonite rather than Ca/Mg carbonates. It means that, apart from the saturation state, the solution stoichiometry may indeed have played at least an auxiliary role in the formation of these and no other carbonates.

The pervasive carbonate formation in GSW is significant for field CO_2 injections into basaltic matrix because it happened so fast; after all the residence time in this flow-through experiment was only 12 h (see table 2). Induction times for nucleation of carbonates are inversely proportional not only to the degree of supersaturation (Olsson, 1995; Söhnel and Mullin, 1988) but also to the concentration of solid particles (Chien et al., 2007). The latter reference found a strong influence of the presence of solid particles on the induction time of $CaCO_3$ at low supersaturation. Based on these findings, it is inferred that the presence of vast amounts of basalt particles together with a substantial degree of carbonate supersaturation (SI of 2.8 and 1.8 for magnesite and calcite, see supplementary material) caused sufficiently fast carbonate nucleation followed by extensive heterogeneous growth. Within only three residence times, ca. 230 m*m* of DIC were immobilised (Fig. 12), followed by an even larger second drop in DIC from 87 to 111 h. If this precipitous decrease in DIC went back to the formation of pure carbonate phases, then the overall drop would correspond to the formation of 2.4 cm^3 of magnesite or 3.1 cm^3 of calcite in the 300 ml reactor (molar volumes of 28 and 37 cm^3/mol assumed). What is more impressive, it means 90% aqueous to solid CO_2 conversion in less than five days, a comparably successful conversion rate like the Carbfix field trial that demonstrated 95% CO_2 mineralisation -however in 400 days (Matter et al., 2016). Because the secondary carbonates formed mainly inside and around the inlet tube of the reactor (where both fluids mixed), the calculated amounts were able to clog the inlet to terminate the experiment prematurely.

The use of seawater for carbonation purposes prior to its injection into the basaltic formation has been discussed previously (Snæbjörnsdottir et al., 2014; Wolff-Boenisch, 2011; Wolff-Boenisch et al., 2011). The advantages of using seawater rather than groundwater for carbonation purposes is that the former is available in quasi-limitless quantities and contains considerable concentrations of divalent Ca and Mg. Furthermore, seawater sulphate also increases basaltic glass dissolution in acid medium by a factor around two-three (Flaathen et al., 2010). In this study, sulphate was deliberately omitted because of its potential to form anhydrite and clog the pores in nature. In natural seawater at 90°C, the SI of anhydrite is -0.4 so anhydrite would not have interfered with carbonate deposition in the GSW experiment because seawater was diluted 2.5 times with the ammonium bicarbonate solution. Yet, in a hypothetical scenario of a seawater carbonated field injection (e.g. into the oceanic crust) anhydrite may, at least at higher temperatures and because of its retrograde solubility, precipitate and consequently scavenge Ca from solution and clog vital pore space. To emphasise the importance of this highly undesirable consequence of using untreated seawater for carbonation, selective removal of sulphate is

routinely carried out in oil production processes where seawater is injected into oilfields to maintain pressure (Bader, 2007). The incompatibility of oil field formation waters and untreated seawater causes sulphate scaling problems (Bader, 2006) that are prevented by extracting the sulphate from the seawater. In the case of CO_2 storage into oceanic basalt beneath the ocean floor, 'scaling' would take place in the basalt pores and reduce injectivity and/or storage capacity. It is unlikely that future field mineralisation efforts are willing to run this risk, all the more as they cannot avoid the formation of smectites and zeolites, so it is anticipated that seawater, if it were used for dissolution of CO_2 prior to injection, would be stripped of sulphate. And although this study covers exclusively the interaction of dissolved aqueous carbon dioxide with the basalt, any injection of dry or undersaturated supercritical CO_2 into a saline sub-oceanic basalt aquifer would entail dry-out processes (Ott et al., 2015), again raising the possibilities for anhydrite formation. Last but not least, sulphate inhibits carbonate formation at higher pH (Flaathen et al., 2011; Mucci et al., 1989) so its presence is detrimental to carbon mineralisation efforts at any rate.

Apart from carbonates, the GSW experiment also yielded secondary silicates, despite the short residence time and the apparent scavenging of divalent cations into carbonates. The tentatively postulated surface coating of chlorite (Fig. 14f) at 90°C is at odds with the work of Gysi and Stefansson (2012b). Whereas these authors did report the occurrence of chlorite in their study on the hydrothermal alteration of basalt under CO_2-rich conditions, they found it at higher T (250 °C) and did not expect it to form below 150 °C. On the other hand, de Caritat et al. (1993) used the reaction of kaolinite+dolomite ↔ chlorite+calcite+CO_2 to establish the stability of a chlorite-carbonate assemblage (the very one ascertained to be present in our GSW experiment) under high(er) pCO_2 conditions and as a function of temperature and found that chlorite-calcite assemblages are already stable at much lower T, clearly below 100°C, depending on the salinity and pCO_2. Applying different geothermometers to a weathered basalt containing chlorite the authors recalculated chlorite formation temperatures between 36 and 107 °C, depending on the applied model.

4.4. Matrix effects on carbon mineralisation

In accord with Gudbrandsson et al. (2011), our reactor experiments showed that dissolution of crystalline and glassy basalt yielded different solution chemistries (Figs. 3,8) and secondary mineralogies (Figs. 5,6), respectively. New dissolution rate equations for glassy as well as crystalline basalt have been developed recently and implemented in reactive transport modelling to account for this fact (Pollyea and Rimstidt, 2017). Likewise, Snæbjörnsdottir et al. (2017a) modelled the solution chemistry and secondary mineralogy of the Carbfix injection and established that the first break-through of the carbonated plume arriving at the monitoring well (via fracture flow) bore the signs of crystalline basalt mobilisation whereas the second larger break-through (via matrix flow) was dominated by basaltic glass dissolution. Notwithstanding these advances in the differentiation of the effects of glassy versus crystalline basalt mobilisation, it still remains problematic to gauge the amount of reactive surfaces from these basalt matrices

that actively contribute to the solution chemistry. The reactive surface area is routinely based on the volume percentage of the individual mineral and glass components in the formation (based on cores or thin sections) but that leaves any larger scale heterogeneities (entire basaltic glass layers or lenses wedged into crystalline formations) or small scale changes (interstitial glass variations) aside. Likewise, within the realm of crystalline basalts, anticipating the most likely secondary carbonate phases of water-CO_2-rock reactions still proves elusive. Schaef et al. (2010) reported significant differences in rates of mineralisation as well as compositions and morphologies of carbonate precipitates that resulted from dissolution of various basalt types under CO_2 injection conditions, although the crystalline basalt specimens (from different geographical provinces) had comparable bulk chemical composition, mineralogy, and dissolution kinetics. Similarly, Kumar et al. (2017) found that dissolution of the crystalline Mandla basalt from the Deccan Trapps under CO_2 storage conditions produced very high calcite yields compared to the Columbia River and Icelandic basalt, despite these basalts exhibiting similar chemical compositions.

It is evident from these findings that lack of crucial information on carbonate and silicate precipitation kinetics and growth rates is still marring our capacity to correctly anticipate what minerals will form in what quantities under what formation and storage conditions. And our study is another example of this deficiency of information. A carbonate like NH_4-dawsonite hardly precipitated in X400 although the solution was patently supersaturated with respect to this mineral (initial SI of 4.5, see supplementary material) whereas the basaltic glass of similar composition yielded much higher NH_4-dawsonite depositions in G400. The solution stoichiometry with respect to the metal cations and carbonate anion was similar in X400 and G400 to rule out a stoichiometry effect, as was the degree of supersaturation (see supplementary material). Stockmann et al. (2014) looked at the effect of different mineral surfaces to catalyse calcite growth and found extensive calcite coatings on olivine, enstatite and peridotite surfaces whereas less calcite formed on labradorite and augite, respectively. The least amenable surface for calcite growth was basaltic glass. These findings suggest that epitaxial growth of calcite should be easier on the compound basalt and its crystalline constituents, notably forsterite but also labradorite and augite, whereas the glass should show the least carbonate growth. Admittedly, NH_4-dawsonite has a different crystal structure (orthorhombic) to calcite (trigonal) so the mineral sequence in which its epitaxial growth is favoured may differ from the one Stockmann et al. (2014) reported for calcite. Still, the glass should be the least growth-promoting carbonate template given its amorphous structure. As such, the glass in experiment G400 should actually have exhibited *less* dawsonite precipitation than its composite counterpart in X400, all else (i.e. pH, T, P, SI, residence time) being the same. On the other hand, more iron oxide formed in G400 which may have acted as crystalline surface sites for heterogeneous nucleation and growth of carbonates to explain this apparent contradiction.

5. Conclusions

Our post-CO_2 injection experiments with glassy (G) and crystalline (X) basalt under neutral to slightly alkaline pH conditions and divalent cation scarcity illustrate that the mono- and divalent

cations obtained from matrix dissolution are scooped up by secondary silicates (G40, X40, G400, X400) and 'non-traditional' dawsonite-type carbonate (G400, X400) rather than the more common carbonates calcite, magnesite, siderite, or ankerite. Supplying, however, extra amounts of mono- and divalent cations to the carbonated solution, from mixing with synthetic seawater, resulted in rapid and massive precipitation of Ca and Mg carbonates in the basaltic glass matrix (GSW), together with a secondary silicate phase which could be chlorite. Both basaltic matrices displayed similarities as well as discrepancies in their secondary mineralogy. What they had in common was the formation of secondary silicate phases, whether smectite (G40/400, X40/400), zeolite (X40/400) or chlorite (GSW), despite the relatively short residence times in the flow-through reactors (25 and 12 h, see table 2). As such, these silicate phases have the potential to scavenge the divalent cations in the basaltic pore space; substantially at low divalent cation concentrations (40 and 400 set) and partially under saline conditions (GSW). Because the experiments were carried out at 90 °C, i.e. likely higher than expected formation temperatures in a basalt aquifer suitable for CO_2 storage, the retrograde solubility of carbonates will only further skew this competition for divalent cations in favour of secondary silicates at lower temperatures. It means that the basaltic aquifer as target formation requires huge storage capacity, not only for the mineralisation of CO_2 but also to accommodate the concomitant and inevitable formation of zeolites and clays. Recent geochemical modelling of basalt-water-CO_2 interactions of the Carbfix site concluded that relatively high pCO_2 conditions needed to be maintained to prevent clay and zeolite formation while at the same time keeping the pH high enough to allow carbonate deposition (Snæbjörnsdottir et al., 2017a). The authors indicated a pH range for efficient carbonatisation between 5.2 and 6.5; however they did not take the ion stoichiometry effect on rates into account, with Me^{2+}/CO_3^{2-} ratios not being favorable at these relatively low pH conditions (Hellevang et al., 2014). Our study went beyond this sweet (pH) spot and looked at the likely consequences to the solutes in the pore fluid –and by extension to the porosity/permeability– after the first wave of plume spreading and secondary phase deposition. Provided shortage of divalent cations, clays and zeolites will occupy the pore space, with preference of one over the other as a function of the nature of the basalt matrix (glass vs. composite). At higher carbonate alkalinity, it is debatable if Na-dawsonite can appear (and subsequently remobilise again). Apparently, the free solute Al concentration was high enough to precipitate dawsonite in our NH_4-rich experiments (G/X400), so its formation in the basalt matrix under divalent cation deficiency will depend on the abundance of Na in the pore water. By and large, however, our experiments point to the prevalence of non-carbonate phases that will occupy the pore space at higher pH and after the spell of carbonatisation. To avoid this from happening, not only the pH needs to remain in a desired range but also the divalent cation concentration should not drop very low. Using treated seawater as carbonation fluid for CO_2 injection provides this pre-requisite; the quasi infinite supply of divalent cations extends the pH range under which carbonates as secondary phases prevail and speeds up the carbonate nucleation and growth process such that better advantage can be taken of the basalt pore volume for carbon, not silicate storage. For this strategy to work successfully, however, reactive transport modelling needs to be implemented on a case by case basis to tune the CO_2 carbonation and injection rates to avoid

clogging of the pore space too close to the injection well. Likewise, potential anhydrite formation requires careful modelling and monitoring after injection to enable sulphate stripping if the need arises.

To this end, further experimental research is needed to advance our understanding of what determines carbonate formation on basaltic surfaces and/or in the basaltic pore space. Despite a plethora of experimental and modelling studies on this subject, recent literature findings indicate that the last word has not yet been said. Luhmann et al. (2017) dissolved a basalt core under hydrothermal CO_2-rich conditions. Whereas siderite was expected to have formed on grounds of reaction path modelling *de facto* observed were secondary Si and Al phases instead. Likewise, Kanakiya et al. (2017) investigated the secondary mineralogy of basalt cores under CO_2(aq) imbibition. Ankerite was indeed the key secondary carbonate phase they observed in their study; however, in one basalt core zeolite/clays instead of ankerite formed, even though the flooding conditions had been the same for all basalts.

More sensitivity analyses on key precipitation parameters (induction time, heterogeneous nucleation and growth rates on diverse crystallographic templates, metal to anion activity ratios, reactive surface areas, and degrees of supersaturation) of carbonates but also sulphates will refine further geochemical models. Fairly recent studies on the reactive surface area of basaltic matrices participating in the mobilisation process (Přikryl et al., 2017), mechanisms of crystal/carbonate growth (Hellevang et al., 2014), and template growth of calcite on basaltic glass (Stockmann et al., 2014) point into the right direction.

Acknowledgements.

We thank the AE Wildgust for handling this manuscript. Insightful comments and constructive reviews by Jonathan Icenhower and Helge Hellevang are also much appreciated and helped improve the quality of this paper. This study is part of the CarbFix project (www.carbfix.com) in Iceland and was funded by the European Union through the European Marie Curie network Delta-Min (Grant PITN-GA-2008-215360) and SP1-Cooperation (FP7-ENERGY-2011-1; Grant 283148), Reykjavik Energy, University of Iceland and RANNIS, Icelandic Fund for Research Equipment; Grant 10/0293 and 121071-0061). The authors would like to thank all colleagues and collaborators from the Carbfix project, University of Iceland and Reykjavik Energy for fruitful discussions during the course of this study.

References

Alfredsson, H.A., Oelkers, E.H., Hardarsson, B.S., Franzson, H., Gunnlaugsson, E., Gislason, S.R., 2013. The geology and water chemistry of the Hellisheidi, SW-Iceland carbon storage site. International Journal of Greenhouse Gas Control 12, 399-418.

Aradóttir, E.S.P., Sonnenthal, E.L., Björnsson, G., Jónsson, H., 2012. Multidimensional reactive transport modeling of CO2 mineral sequestration in basalts at the Hellisheidi geothermal field, Iceland. International Journal of Greenhouse Gas Control 9, 24-40.

Bader, M.S.H., 2006. Sulfate scale problems in oil fields water injection operations. Desalination 201, 100-105.
Bader, M.S.H., 2007. Sulfate removal technologies for oil fields seawater injection operations. Journal of Petroleum Science and Engineering 55, 93-110.
Baker, J.C., Bai, G.P., Hamilton, P.J., Golding, S.D., Keene, J.B., 1995. Continental-scale magmatic carbon dioxide seepage recorded by dawsonite in the Bowen-Gunnedah-Sydney Basin system, eastern Australia. Journal of Sedimentary Research 65, 522.
Baker, P.A., Stout, P.M., Kastner, M., Elderfield, H., 1991. Large-Scale Lateral Advection of Seawater through Oceanic-Crust in the Central Equatorial Pacific. Earth and Planetary Science Letters 105, 522-533.
Bénézeth, P., Palmer, D.A., Anovitz, L.M., Horita, J., 2007. Dawsonite synthesis and reevaluation of its thermodynamic properties from solubility measurements: Implications for mineral trapping of CO2. Geochimica et Cosmochimica Acta 71, 4438-4455.
Brunauer, S., Emmett, P.H., Teller, E., 1938. Adsorption of Gases in Multimolecular Layers. Journal of the American Chemical Society 60, 309-319.
Chhim, N., Kharbachi, C., Neveux, T., Bouteleux, C., Teychené, S., Biscans, B., 2017. Inhibition of calcium carbonate crystal growth by organic additives using the constant composition method in conditions of recirculating cooling circuits. Journal of Crystal Growth 472, 35-45.
Chien, W.-C., Lee, C.-C., Tai, C.Y., 2007. Heterogeneous Nucleation Rate of Calcium Carbonate Derived from Induction Period. Industrial & Engineering Chemistry Research 46, 6435-6441.
de Caritat, P., Hutcheon, I., Walshe, J.L., 1993. Chlorite geothermometry; a review. Clays and Clay Minerals 41, 219.
Flaathen, T.K., Gislason, S.R., Oelkers, E.H., 2010. The effect of aqueous sulphate on basaltic glass dissolution rates. Chemical Geology 277, 345-354.
Flaathen, T.K., Oelkers, E.H., Gislason, S.R., Aagaard, P., 2011. The effect of dissolved sulphate on calcite precipitation kinetics and consequences for subsurface CO2 storage. Energy Procedia 4, 5037-5043.
Fouillac, A.M., Fouillac, C., Cesbron, F., Pillard, F., Legendre, O., 1989. Water-rock interaction between basalt and high-salinity fluids in the Asal Rift, Republic of Djibouti. Chemical Geology 76, 271-289.
Galeczka, I., Wolff-Boenisch, D., Oelkers, E.H., Gislason, S.R., 2014. An experimental study of basaltic glass–H2O–CO2 interaction at 22 and 50 °C: Implications for subsurface storage of CO2. Geochimica et Cosmochimica Acta 126, 123-145.
Gao, Y., Liu, L., Hu, W., 2009. Petrology and isotopic geochemistry of dawsonite-bearing sandstones in Hailaer basin, northeastern China. Applied Geochemistry 24, 1724-1738.
Gislason, S.R., Broecker, W.S., Gunnlaugsson, E., Snæbjörnsdóttir, S., Mesfin, K.G., Alfredsson, H.A., Aradottir, E.S., Sigfusson, B., Gunnarsson, I., Stute, M., Matter, J.M., Arnarson, M.T., Galeczka, I.M., Gudbrandsson, S., Stockman, G., Boenisch, D.W., Stefansson, A., Ragnheidardottir, E., Flaathen, T., Gysi, A.P., Olssen, J., Didriksen, K., Stipp, S., Menez, B., Oelkers, E.H., 2014. Rapid solubility and mineral storage of CO2 in basalt. Energy Procedia 63, 4561-4574.
Gislason, S.R., Oelkers, E.H., 2003. Mechanism, rates, and consequences of basaltic glass dissolution: II. An experimental study of the dissolution rates of basaltic glass as a function of pH and temperature. Geochimica et Cosmochimica Acta 67, 3817-3832.
Gislason, S.R., Oelkers, E.H., 2014. Carbon Storage in Basalt. Science 344, 373.
Golab, A.N., Carr, P.F., Palamara, D.R., 2006. Influence of localised igneous activity on cleat dawsonite formation in Late Permian coal measures, Upper Hunter Valley, Australia. International Journal of Coal Geology 66, 296-304.
Gudbrandsson, S., Wolff-Boenisch, D., Gislason, S.R., Oelkers, E.H., 2011. An experimental study of crystalline basalt dissolution from 2 ≤ pH ≤ 11 and temperatures from 5 to 75 C. Geochim Cosmochim Acta 75.

Gysi, A.P., Stefansson, A., 2011. CO2–water–basalt interaction. Numerical simulation of low temperature CO2 sequestration into basalts. Geochimica et Cosmochimica Acta 75, 4728-4751.
Gysi, A.P., Stefansson, A., 2012a. CO2-water–basalt interaction. Low temperature experiments and implications for CO2 sequestration into basalts. Geochimica et Cosmochimica Acta 81, 129-152.
Gysi, A.P., Stefansson, A., 2012b. Mineralogical aspects of CO2 sequestration during hydrothermal basalt alteration — An experimental study at 75 to 250 °C and elevated pCO2. Chemical Geology 306–307, 146-159.
Hangx, S.J.T., Spiers, C.J., 2009. Reaction of plagioclase feldspars with CO2 under hydrothermal conditions. Chemical Geology 265, 88-98.
Hellevang, H., Declercq, J., Aagaard, P., 2011. Why is dawsonite absent in CO2 charged reservoirs? Oil & Gas Science and Technology - Re. IFP Energies nouvelles 66.
Hellevang, H., Haile, B.G., Tetteh, A., 2017. Experimental study to better understand factors affecting the CO2 mineral trapping potential of basalt. Greenhouse Gases: Science and Technology 7, 143-157.
Hellevang, H., Miri, R., Haile, B.G., 2014. New Insights into the Mechanisms Controlling the Rate of Crystal Growth. Crystal Growth & Design 14, 6451-6458.
Hong, M., Teng, H.H., 2014. Implications of solution chemistry effects: Direction-specific restraints on the step kinetics of calcite growth. Geochimica et Cosmochimica Acta 141, 228-239.
IEA, 2015. World Energy Outlook Special Report: Energy and Climate Change – Executive Summary. IEA, France.
IPCC, 2014. Climate Change 2014: Mitigation of Climate Change. Contribution of Working Group III to the Fifth Assessment Report of the Intergovernmental Panel on Climate Change, in: Edenhofer, O., R. Pichs-Madruga, Y. Sokona, E. Farahani, S. Kadner, K. Seyboth, A. Adler, I. Baum, S. Brunner, P. Eickemeier, B. Kriemann, J. Savolainen, S. Schlömer, C. von Stechow, T. Zwickel and J.C. Minx (Ed.), Cambridge University Press, Cambridge, United Kingdom and New York, NY, USA.
Kanakiya, S., Adam, L., Esteban, L., Rowe, M.C., Shane, P., 2017. Dissolution and secondary mineral precipitation in basalts due to reactions with carbonic acid. Journal of Geophysical Research: Solid Earth 122, 4312-4327.
Kaszuba, J.P., Janecky, D.R., Snow, M.G., 2005. Experimental evaluation of mixed fluid reactions between supercritical carbon dioxide and NaCl brine: Relevance to the integrity of a geologic carbon repository. Chemical Geology 217, 277-293.
Kaszuba, J.P., Viswanathan, H.S., Carey, J.W., 2011. Relative stability and significance of dawsonite and aluminum minerals in geologic carbon sequestration. Geophysical Research Letters 38, n/a-n/a.
Knauss, K.G., Johnson, J.W., Steefel, C.I., 2005. Evaluation of the impact of CO2, co-contaminant gas, aqueous fluid and reservoir rock interactions on the geologic sequestration of CO2. Chemical Geology 217, 339-350.
Kumar, A., Shrivastava, J.P., Pathak, V., 2017. Mineral carbonation reactions under water-saturated, hydrothermal-like conditions and numerical simulations of CO2 sequestration in tholeiitic basalt of the Eastern Deccan Volcanic Province, India. Applied Geochemistry 84, 87-104.
Labus, K., Bujok, P., 2011. CO2 mineral sequestration mechanisms and capacity of saline aquifers of the Upper Silesian Coal Basin (Central Europe) - Modeling and experimental verification. Energy 36, 4974-4982.
Larsen, K., Bechgaard, K., Stipp, S.L.S., 2010. The effect of the Ca2+ to activity ratio on spiral growth at the calcite surface. Geochimica et Cosmochimica Acta 74, 2099-2109.
Lodziana, Z., Stoica, G., Pérez-Ramírez, J., 2011. Reevaluation of the Structure and Fundamental Physical Properties of Dawsonites by DFT Studies. Inorganic Chemistry 50, 2590-2598.
Luhmann, A.J., Tutolo, B.M., Tan, C., Moskowitz, B.M., Saar, M.O., Seyfried Jr, W.E., 2017. Whole rock basalt alteration from CO2-rich brine during flow-through experiments at 150 °C and 150 bar. Chemical Geology 453, 92-110.

Matter, J.M., Stute, M., Snæbjörnsdottir, S.Ó., Oelkers, E.H., Gislason, S.R., Aradottir, E.S., Sigfusson, B., Gunnarsson, I., Sigurdardottir, H., Gunnlaugsson, E., Axelsson, G., Alfredsson, H.A., Wolff-Boenisch, D., Mesfin, K., Taya, D.F.d.l.R., Hall, J., Dideriksen, K., Broecker, W.S., 2016. Rapid carbon mineralization for permanent disposal of anthropogenic carbon dioxide emissions. Science 352, 1312.

McGrail, B.P., Schaef, H.T., Spane, F.A., Cliff, J.B., Qafoku, O., Horner, J.A., Thompson, C.J., Owen, A.T., Sullivan, C.E., 2017. Field Validation of Supercritical CO2 Reactivity with Basalts. Environmental Science & Technology Letters 4, 6-10.

Millero, F.J., 2003. Physicochemical Controls on Seawater, in: Holland, H., D., Turekian, K., K. (Eds.), Treatise on Geochemistry. Pergamon, Oxford, pp. 1-21.

Mohd Amin, S., Weiss, D.J., Blunt, M.J., 2014. Reactive transport modelling of geologic CO2 sequestration in saline aquifers: The influence of pure CO2 and of mixtures of CO2 with CH4 on the sealing capacity of cap rock at 37 °C and 100 bar. Chemical Geology 367, 39-50.

Mucci, A., Canuel, R., Zhong, S., 1989. The solubility of calcite and aragonite in sulfate-free seawater and the seeded growth kinetics and composition of the precipitates at 25°C. Chemical Geology 74, 309-320.

Nehrke, G., Reichart, G.J., Van Cappellen, P., Meile, C., Bijma, J., 2007. Dependence of calcite growth rate and Sr partitioning on solution stoichiometry: Non-Kossel crystal growth. Geochimica et Cosmochimica Acta 71, 2240-2249.

Oelkers, E.H., Gislason, S.R., 2001. The mechanism, rates and consequences of basaltic glass dissolution: I. An experimental study of the dissolution rates of basaltic glass as a function of aqueous Al, Si and oxalic acid concentration at 25°C and pH = 3 and 11. Geochimica et Cosmochimica Acta 65, 3671-3681.

Olsson, L.-F., 1995. Induction time of precipitation of calcium carbonate. Studies in Physical and Theoretical Chemistry 83, 349-352.

Ott, H., Roels, S.M., de Kloe, K., 2015. Salt precipitation due to supercritical gas injection: I. Capillary-driven flow in unimodal sandstone. International Journal of Greenhouse Gas Control 43, 247-255.

Parkhurst, D.L., Appelo, C.A.J., 1999. User's guide to PHREEQC (Version 2)--a computer program for speciation, batch-reaction, one-dimensional transport, and inverse geochemical calculations, U.S. Geological Survey Water-Resources Investigations Report 99-4259, p.310.

Parkhurst, D.L., Appelo, C.A.J., 2013. Description of input and examples for PHREEQC version 3—A computer program for speciation, batch-reaction, one-dimensional transport, and inverse geochemical calculations, U.S. Geological Survey Techniques and Methods, p. 497.

Perdikouri, C., Putnis, C.V., Kasioptas, A., Putnis, A., 2009. An Atomic Force Microscopy Study of the Growth of a Calcite Surface as a Function of Calcium/Total Carbonate Concentration Ratio in Solution at Constant Supersaturation. Crystal Growth & Design 9, 4344-4350.

Pham, T.H., Aagaard, P., Hellevang, H., 2012. On the potential for CO2 mineral storage in continental flood basalts – PHREEQC batch- and 1D diffusion–reaction simulations. Geochemical Transactions 13, 5.

Pham, V.T.H., Lu, P., Aagaard, P., Zhu, C., Hellevang, H., 2011. On the potential of CO2-water-rock interactions for CO2 storage using a modified kinetic model. International Journal of Greenhouse Gas Control 5.

Pokrovsky, O.S., Schott, J., 2000. Kinetics and mechanism of forsterite dissolution at 25°C and pH from 1 to 12. Geochimica et Cosmochimica Acta 64, 3313-3325.

Pollyea, R.M., Rimstidt, J.D., 2017. Rate equations for modeling carbon dioxide sequestration in basalt. Applied Geochemistry 81, 53-62.

Přikryl, J., Jha, D., Stefánsson, A., Stipp, S.L.S., 2017. Mineral dissolution in porous media: An experimental and modeling study on kinetics, porosity and surface area evolution. Applied Geochemistry in press.

Rogers, K.L., Neuhoff, P.S., Pedersen, A.K., Bird, D.K., 2006. CO2 metasomatism in a basalt-hosted petroleum reservoir, Nuussuaq, West Greenland. Lithos 92, 55-82.

Rosenbauer, R.J., Thomas, B., Bischoff, J.L., Palandri, J., 2012. Carbon sequestration via reaction with basaltic rocks: Geochemical modeling and experimental results. Geochimica et Cosmochimica Acta 89, 116-133.
Saar, M.O., Manga, M., 1999. Permeability-porosity relationship in vesicular basalts. Geophysical Research Letters 26, 111-114.
Schaef, H.T., McGrail, B.P., Owen, A.T., 2010. Carbonate mineralization of volcanic province basalts. International Journal of Greenhouse Gas Control 4, 249-261.
Schaef, H.T., McGrail, B.P., Owen, A.T., Arey, B.W., 2013. Mineralization of basalts in the CO2–H2O–H2S system. International Journal of Greenhouse Gas Control 16, 187-196.
Snæbjörnsdottir, S., Gislason, S.R., Galeczka, I., Oelkers, E.H., 2017a. Reaction path modelling of in-situ mineralisation of CO2 at the CarbFix site in SW-Iceland. . Geochimica et Cosmochimica Acta, accepted.
Snæbjörnsdottir, S.Ó., Oelkers, E.H., Mesfin, K., Aradóttir, E.S., Dideriksen, K., Gunnarsson, I., Gunnlaugsson, E., Matter, J.M., Stute, M., Gislason, S.R., 2017b. The chemistry and saturation states of subsurface fluids during the in situ mineralisation of CO2 and H2S at the CarbFix site in SW-Iceland. International Journal of Greenhouse Gas Control 58, 87-102.
Snæbjörnsdottir, S.Ó., Wiese, F., Fridriksson, T., Ármansson, H., Einarsson, G.M., Gislason, S.R., 2014. CO2 storage potential of basaltic rocks in Iceland and the oceanic ridges. Energy Procedia 63, 4585-4600.
Söhnel, O., Mullin, J.W., 1988. Interpretation of crystallization induction periods. Journal of Colloid and Interface Science 123, 43-50.
Sonnenthal, E., Ito, A., Spycher, N., Yui, M., Apps, J., Sugita, Y., Conrad, M., Kawakami, S., 2005. Approaches to modeling coupled thermal, hydrological, and chemical processes in the drift scale heater test at Yucca Mountain. International Journal of Rock Mechanics and Mining Sciences 42, 698-719.
Steefel, C.I., Beckingham, L.E., Landrot, G., 2015. Micro-Continuum Approaches for Modeling Pore-Scale Geochemical Processes. Reviews in Mineralogy and Geochemistry 80, 217.
Stockmann, G., Wolff-Boenisch, D., Gislason, S.R., Oelkers, E.H., 2011. Do carbonate precipitates affect dissolution kinetics? 1: Basaltic glass. Chemical Geology accepted.
Stockmann, G.J., Wolff-Boenisch, D., Bovet, N., Gislason, S.R., Oelkers, E.H., 2014. The role of silicate surfaces on calcite precipitation kinetics. Geochimica et Cosmochimica Acta 135, 231-250.
Tambach, T.J., Koenen, M., Wasch, L.J., van Bergen, F., 2015. Geochemical evaluation of CO2 injection and containment in a depleted gas field. International Journal of Greenhouse Gas Control 32, 61-80.
Wilkinson, M., Haszeldine, R.S., Fallick, A.E., Odling, N., Stoker, S.J., Gatliff, R.W., 2009. CO2-Mineral Reaction in a Natural Analogue for CO2 Storage -Implications for Modeling. Journal of Sedimentary Research 79, 486.
Wolff-Boenisch, D., 2011. On the buffer capacity of CO2 -charged seawater used for carbonation and subsequent mineral sequestration. Energy Procedia 4, 3738-3745.
Wolff-Boenisch, D., Galeczka, I.M., Mesfin, K.G., Gislason, S.R., 2016. A foray into false positive results in mineral dissolution and precipitation studies. Applied Geochemistry 71, 9-19.
Wolff-Boenisch, D., Wenau, S., Gislason, S.R., Oelkers, E.H., 2011. Dissolution of basalts and peridotite in seawater, in the presence of ligands, and CO2: Implications for mineral sequestration of carbon dioxide. Geochimica et Cosmochimica Acta 75, 5510-5525.
Worden, R.H., 2006. Dawsonite cement in the Triassic Lam Formation, Shabwa Basin, Yemen: A natural analogue for a potential mineral product of subsurface CO2 storage for greenhouse gas reduction. Marine and Petroleum Geology 23, 61-77.
Xu, T., Apps, J.A., Pruess, K., 2004. Numerical simulation of CO2 disposal by mineral trapping in deep aquifers. Applied Geochemistry 19, 917-936.
Xu, T., Apps, J.A., Pruess, K., Yamamoto, H., 2007. Numerical modeling of injection and mineral trapping of CO2 with H2S and SO2 in a sandstone formation. Chemical Geology 242, 319-346.

Xu, T., Kharaka, Y.K., Doughty, C., Freifeld, B.M., Daley, T.M., 2010. Reactive transport modeling to study changes in water chemistry induced by CO2 injection at the Frio-I Brine Pilot. Chemical Geology 271, 153-164.
You, C.-F., Chan, L.H., Gieskes, J.M., Klinkhammer, G.P., 2003. Seawater intrusion through the oceanic crust and carbonate sediment in the Equatorial Pacific: Lithium abundance and isotopic evidence. Geophysical Research Letters 30, n/a-n/a.
Zerai, B., Saylor, B.Z., Matisoff, G., 2006. Computer simulation of CO2 trapped through mineral precipitation in the Rose Run Sandstone, Ohio. Applied Geochemistry 21, 223-240.
Zuddas, P., Mucci, A., 1994. Kinetics of calcite precipitation from seawater: I. A classical chemical kinetics description for strong electrolyte solutions. Geochimica et Cosmochimica Acta 58, 4353-4362.

Basaltic rock	Chemical composition	A_{BET} (m^2/g)
Glass	$Si_{1.0}Ti_{0.024}Al_{0.355}Mg_{0.276}Ca_{0.265}Na_{0.073}K_{0.007}Fe_{0.207}O_{3.381}$	2.2
Crystalline	$Si_{1.0}Ti_{0.025}Al_{0.329}Mg_{0.310}Ca_{0.273}Na_{0.061}K_{0.007}Fe(III)_{0.02}Fe(II)_{0.193}O_{3.394}$	0.7

Table 1. Chemical composition (normalised to one silicon) and surface areas of the basaltic glass and crystalline basalt used in this study. Data are from Galezcka et al. (2014) and Gudbrandsson et al. (2011).

Name	NH_4HCO_3 [mmol/kg]	Temp [°C]	pH insitu	Flow rate [ml/min]	Mass [g]	Size fraction [µm]	Mixing speed [rpm]	Duration [h]
G40	40	90	~7	0.2	7	45-100	90	1176
X40	40	90	~7	0.2	7	45-125	90	1176
G400	400	90	~7.7	0.2	7	45-100	90	1633
X400	400	90	~7.7	0.2	7	45-125	90	1633
GSW	315	90	~7.2	0.3+0.12	7	45-100	90	111

Table 2. Experimental parameters for the basaltic glass (G) and crystalline basalt (X) mixed flow reactor experiments. The reactor volume was 300 ml corresponding to a residence time of 25 h for all experiments except the last one, where it was 12 h.

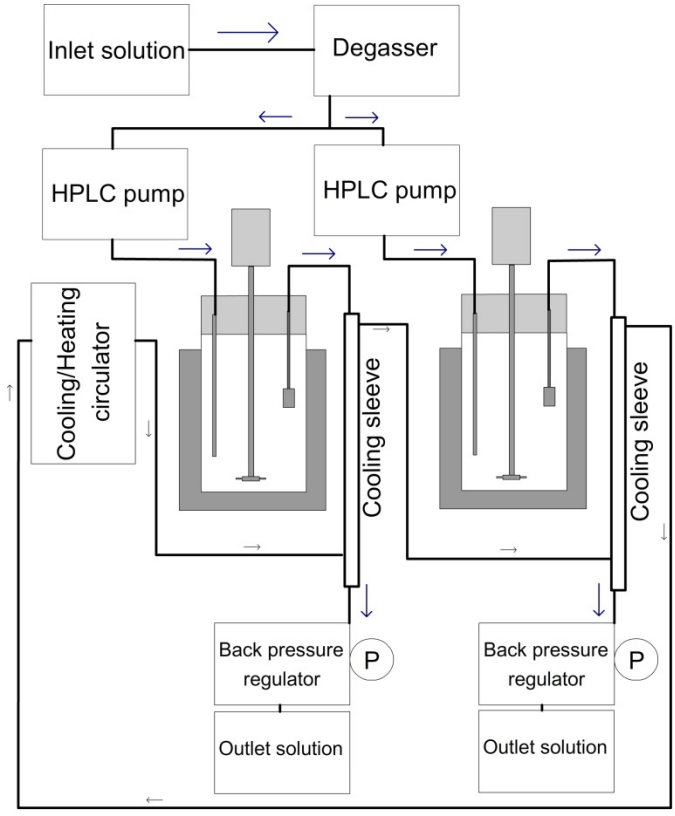

Figure 1. Experimental set-up of the glassy (G) and crystalline (X) basalt experiments. Glass and crystalline basalt were dissolved separately in a Parr reactor each. See Table 2 for further experimental conditions.

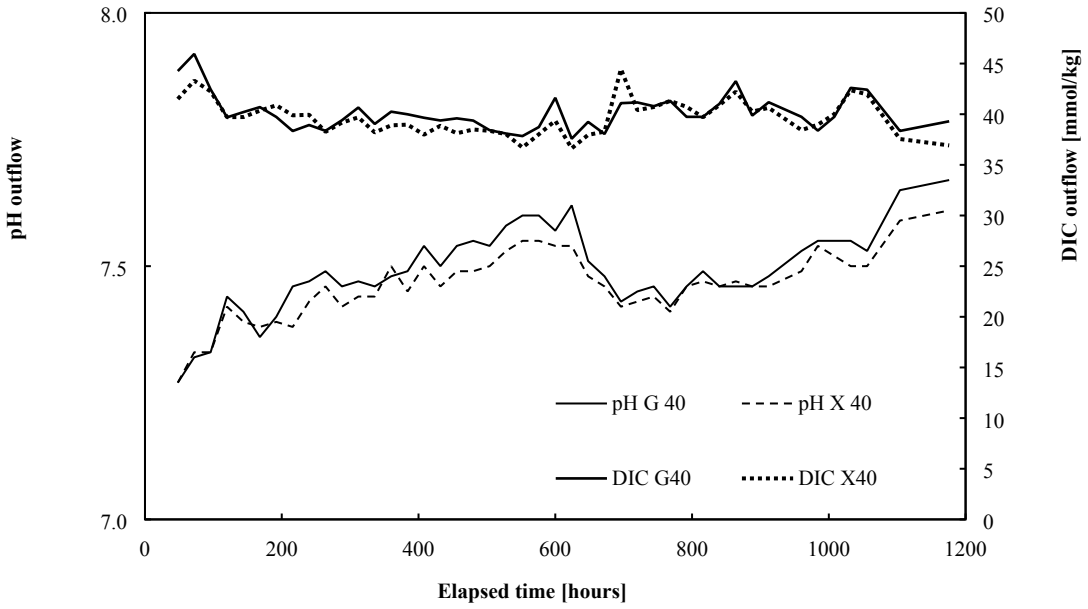

Figure 2. The pH (left axis) and DIC (right axis) from the outlet of the basaltic glass (G40) and crystalline basalt (X40) experiments (see Table 2). The residence time of the inlet solution within the reactor was 25 h.

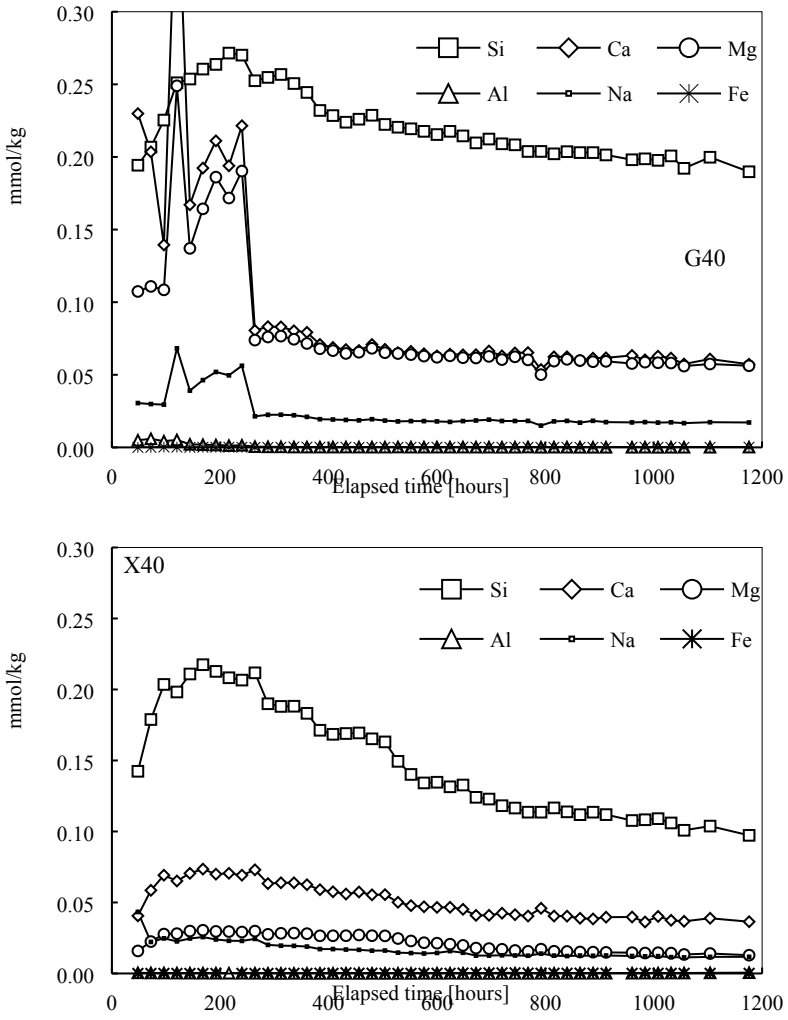

Figure 3. Chemistry of outlet solutions of the basaltic glass (G40) and crystalline basalt (X40) experiments (see Table 2).

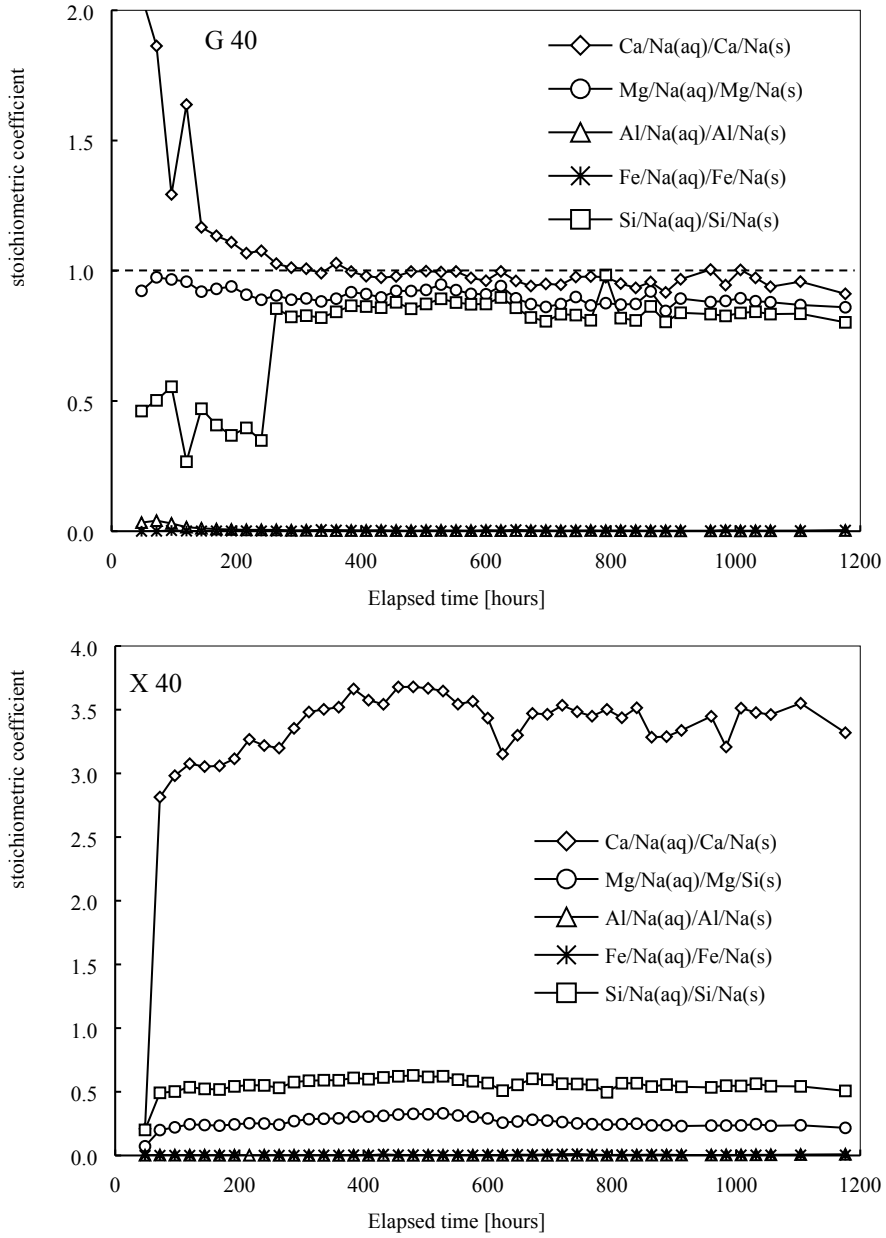

Figure 4. Non-stoichiometry of the dissolution of the basaltic glass (G40) and crystalline basalt (X40) experiments (see Table 2).

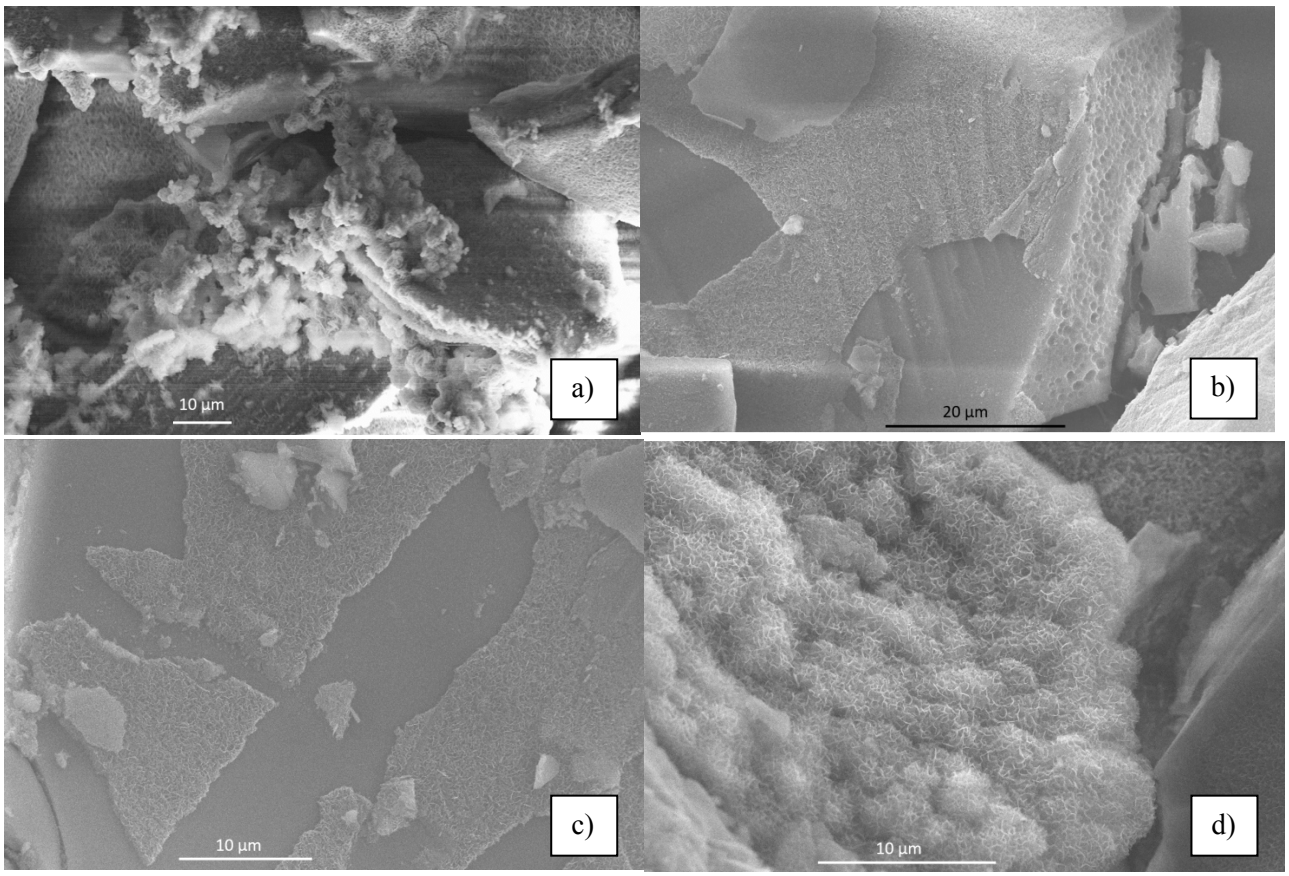

Figure 5. SEM micrographs from the basaltic glass experiment G40 showing iron precipitations on the glass surface in the shape of (a) sphere clusters and (b-c) incorporated into a thin silicate layer. EDX together with XRD and textural comparisons with findings from Gysi and Stefansson (2012) suggest this layer to be a Fe-Mg smectite. (d) Close-up of the smectite layer.

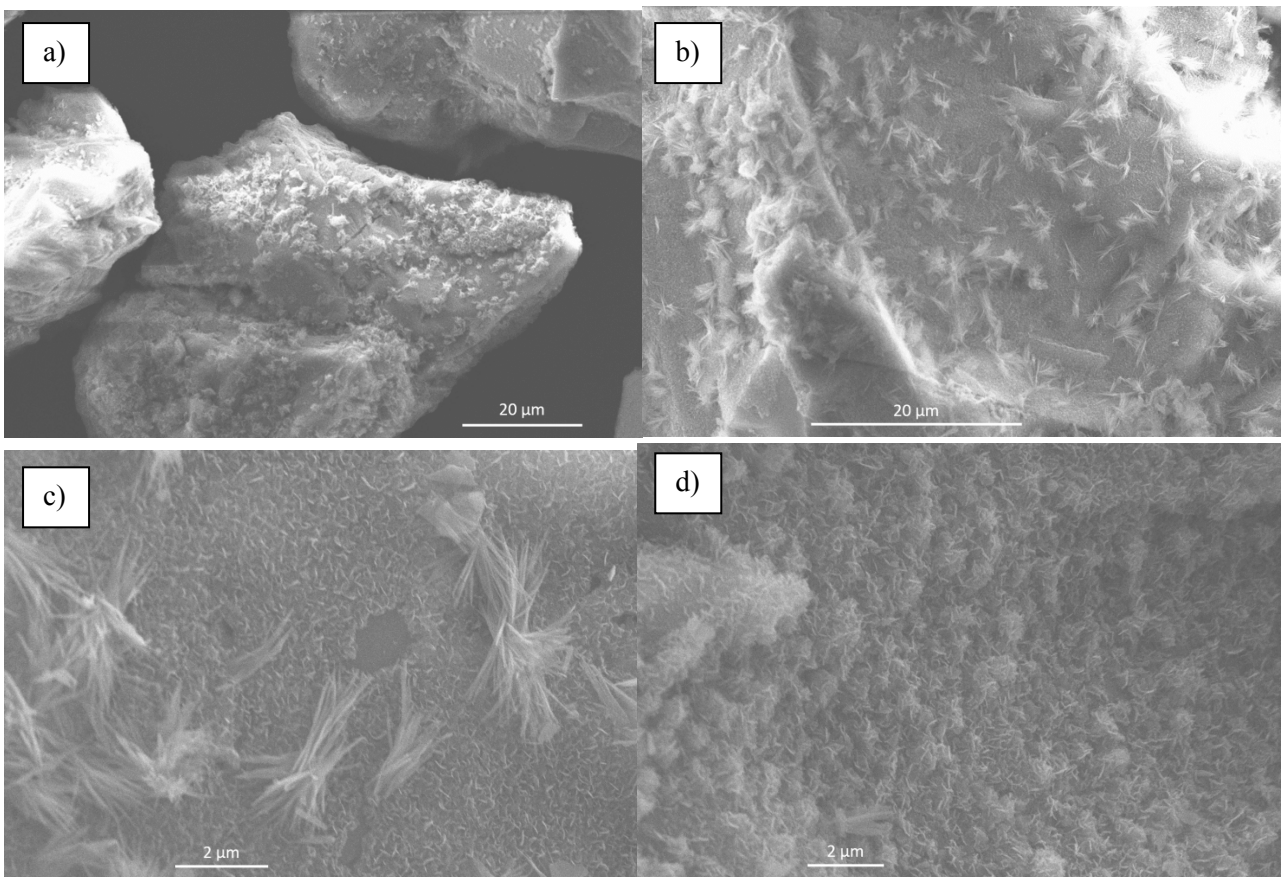

Figure 6. SEM micrographs from the crystalline basalt experiment X40. (a-b) Silicate precipitations in the shape of bunches of needles cropping up from the surface. (c) Close-up revealing two different phases, a thin secondary layer and needle clusters. (d) Secondary silicates similar in appearance and EDX to Fig. 5d.

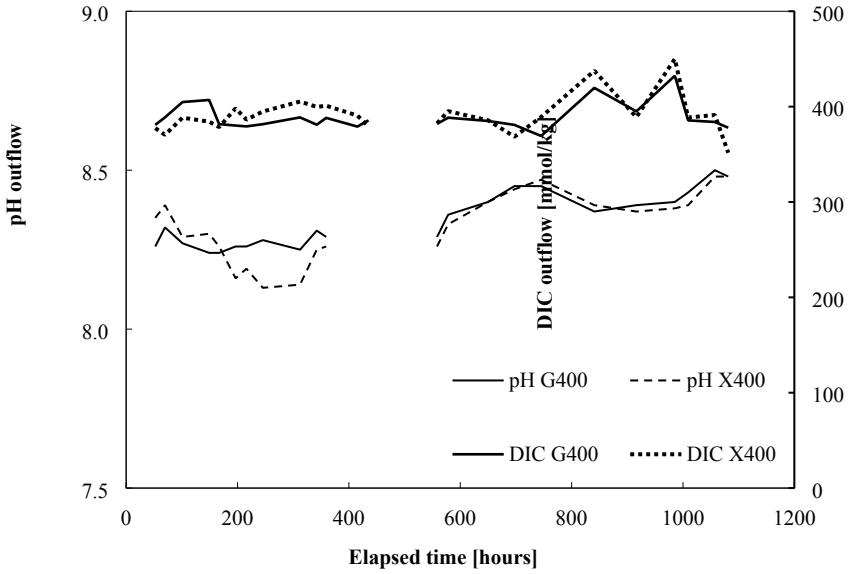

Figure 7. The pH (left axis) and DIC (right axis) from the outlet of the basaltic glass (G400) and crystalline basalt (X400) experiments (see Table 2).

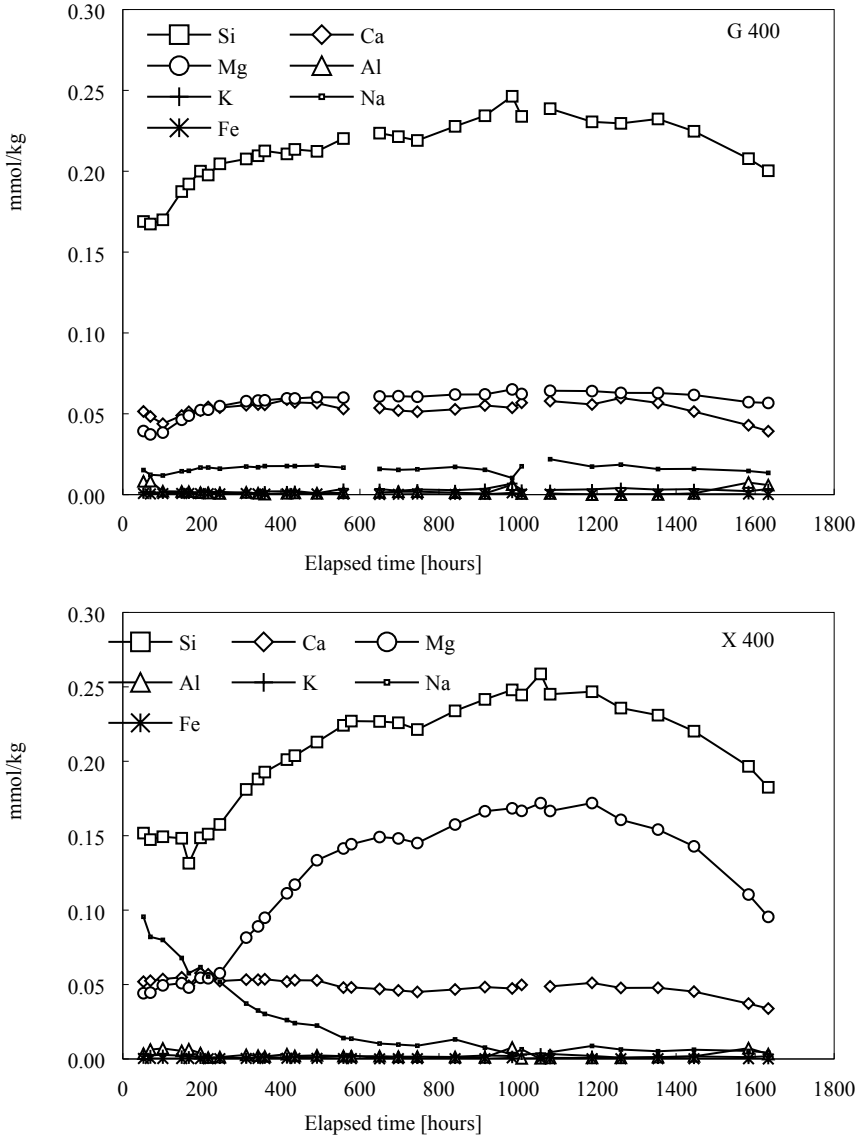

Figure 8. Solute concentrations from the outflow of the basaltic glass (G400) and crystalline basalt (X400) experiments (see Table 2).

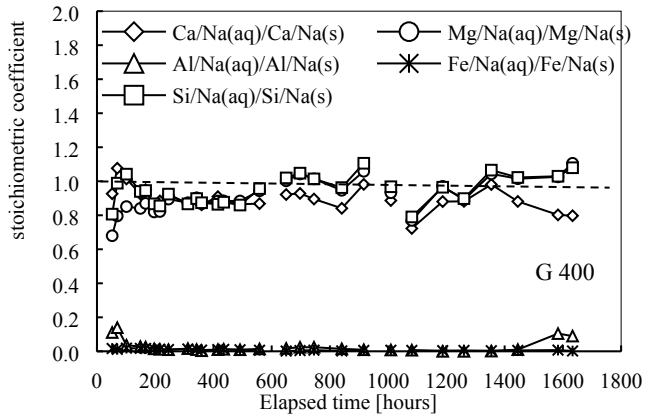

Figure 9. Non-stoichiometry of the dissolution of the basaltic glass experiment G400 (see Table 2).

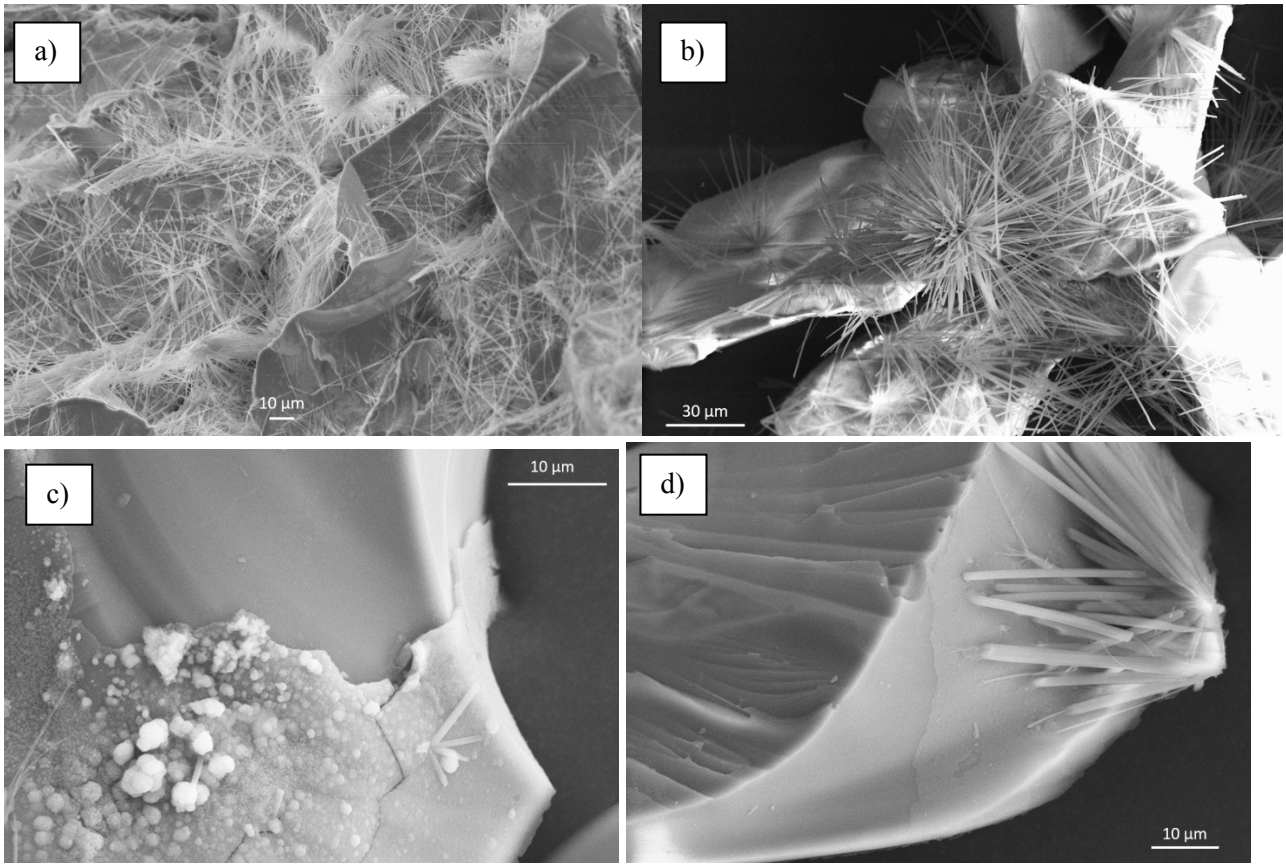

Figure 10. SEM micrographs from the basaltic glass experiment G400 showing the different secondary phases that formed on the glass surface. (a) Scattered dawsonite needles, (b) Dawsonite bunches, (c) Iron oxide pellets, (d) Thin glass surface coating next to a dawsonite stack.

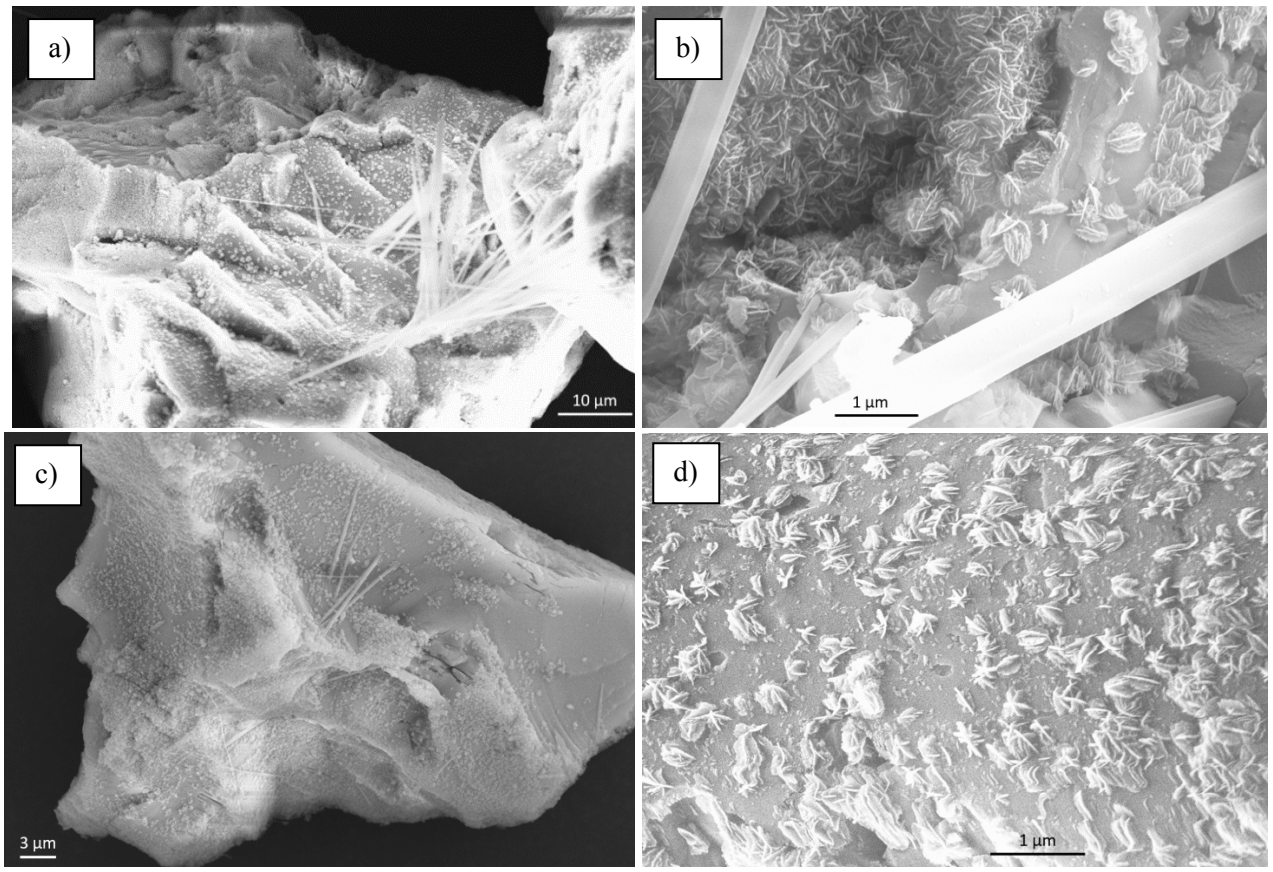

Figure 11. SEM micrographs from the crystalline basalt experiment X400 showing the different secondary phases that formed. (a) Dawsonite needles, (b) Iron oxide balls (of wool), (c) Individually scattered bunches, (d) Close-up of the bunches that are similar to those in Fig. 6a-c.

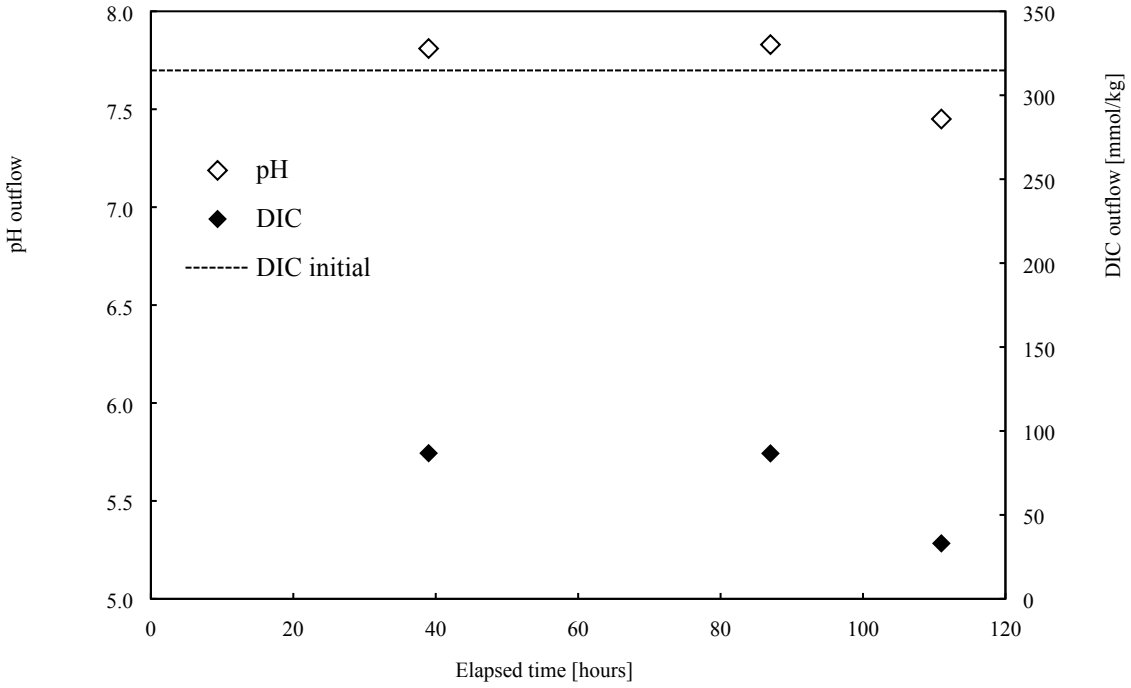

Figure 12. The pH (left axis depicted by open diamonds) and DIC (right axis depicted by filled diamonds) from the outlet of the basaltic glass experiment GSW (see Table 2). The DIC entering the reactor is indicated by the dashed line.

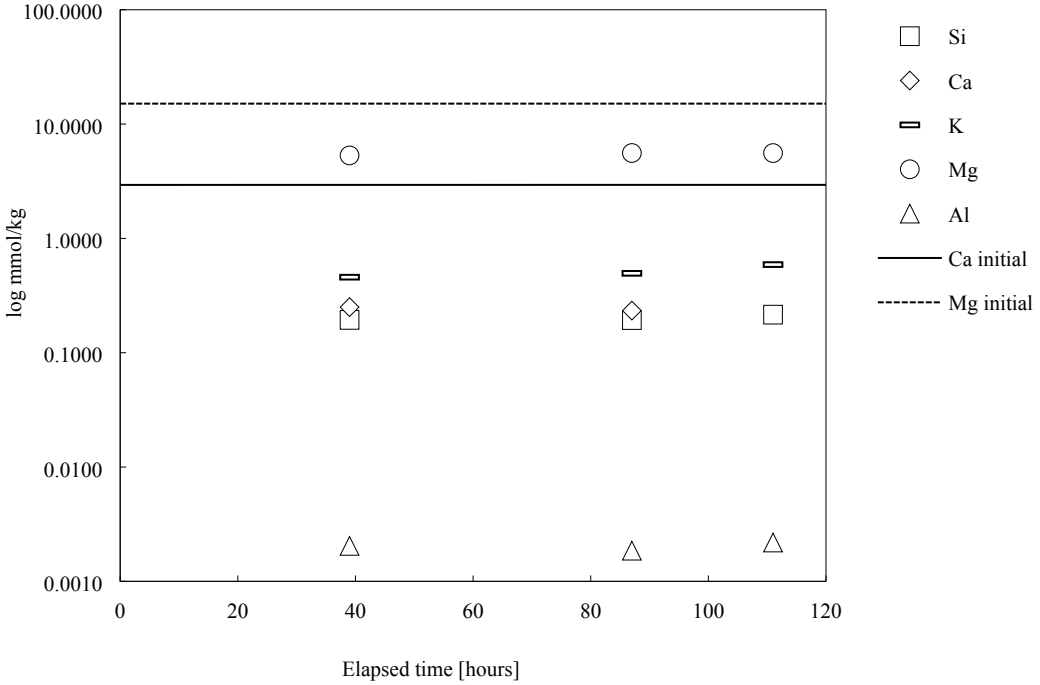

Figure 13. Solute concentrations from the outflow of the basaltic glass experiment GSW (see Table 2). The Ca and Mg concentrations entering the reactor are indicated by the dashed lines.

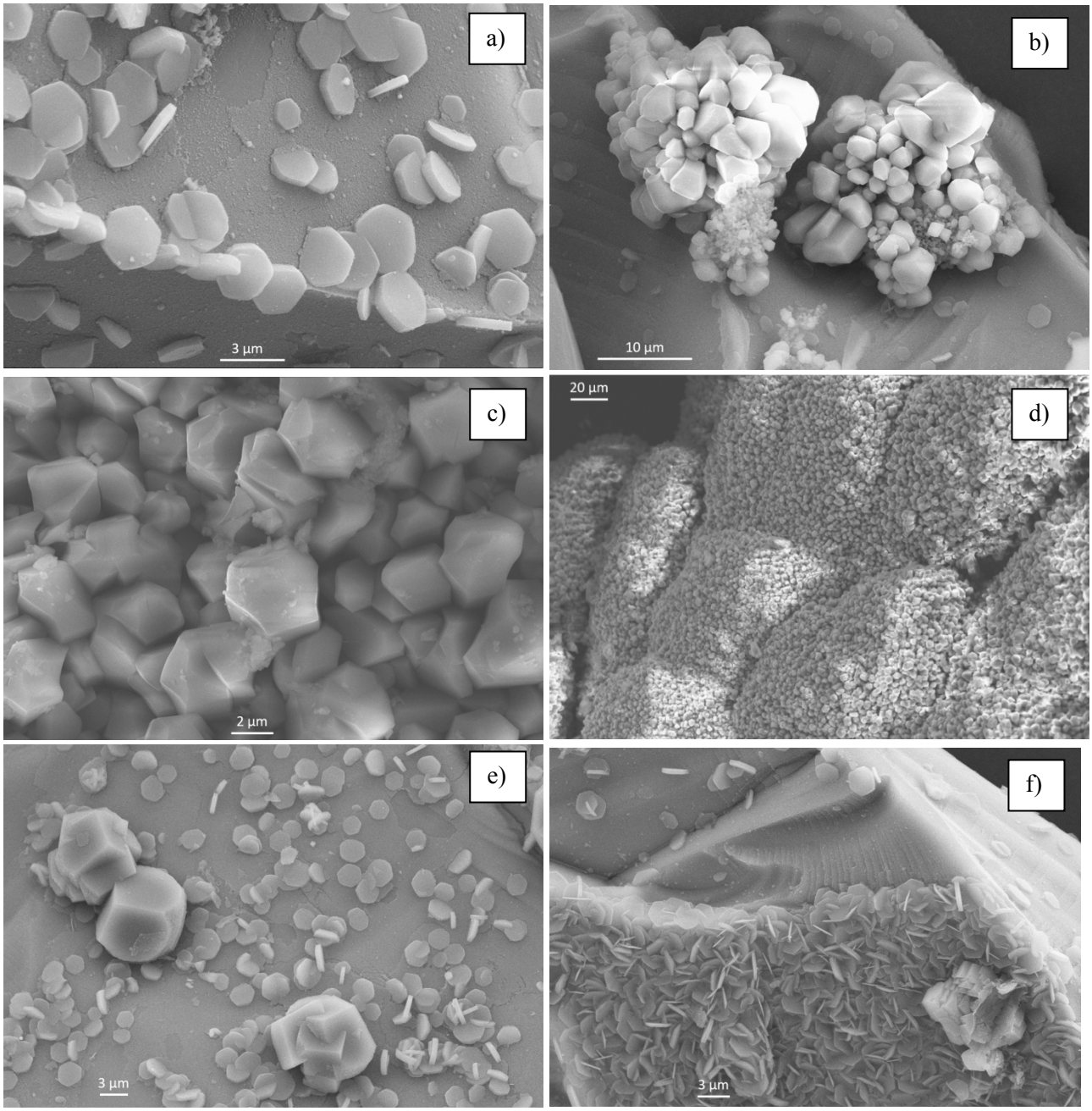

Figure 14. SEM micrographs from the basaltic glass-seawater experiment GSW showing the ubiquitous presence of carbonates. (a-c) Rhombohedral crystals indicating calcite, (d) globular-like manifestation of Ca-carbonate, (e) Mg-carbonates, (f) Flaky silicate matrix reminiscent of chlorite.

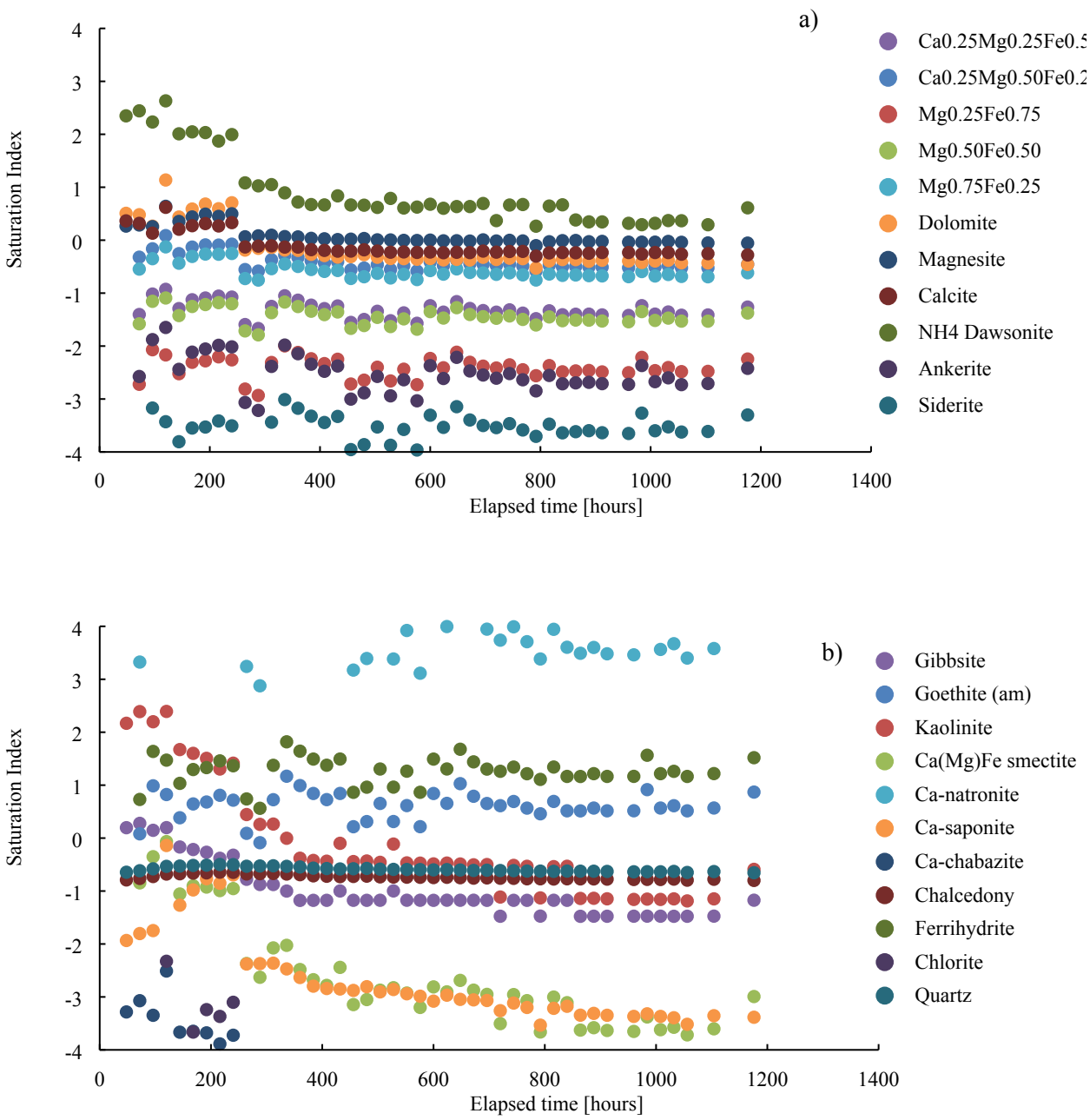

Figure 1. Saturation indices of the major (a) carbonate and (b) silicate phases of the G40 experiment (see Table 2).

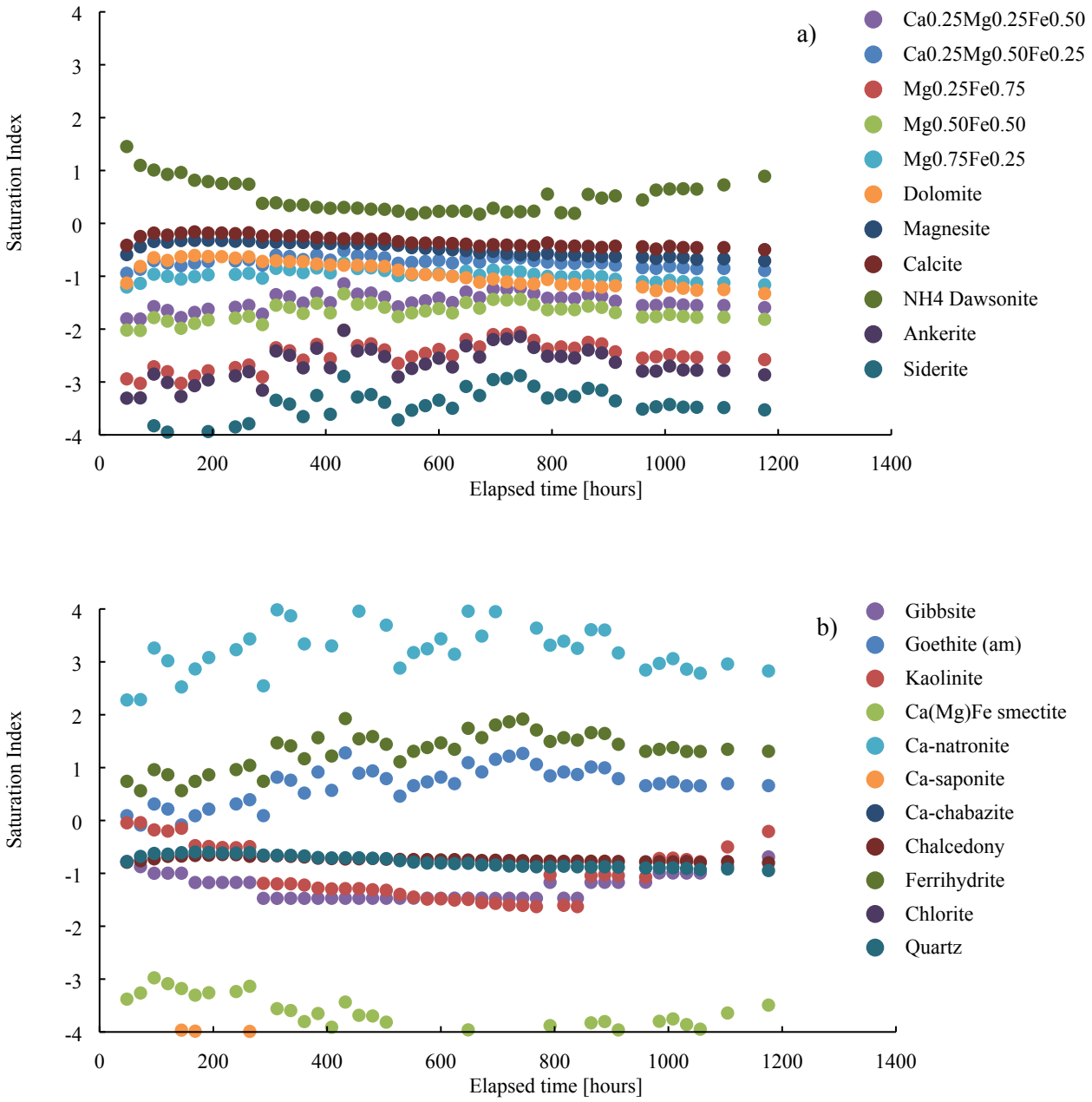

Figure 2. Saturation indices of the major (a) carbonate and (b) silicate phases of the X40 experiment (see Table 2).

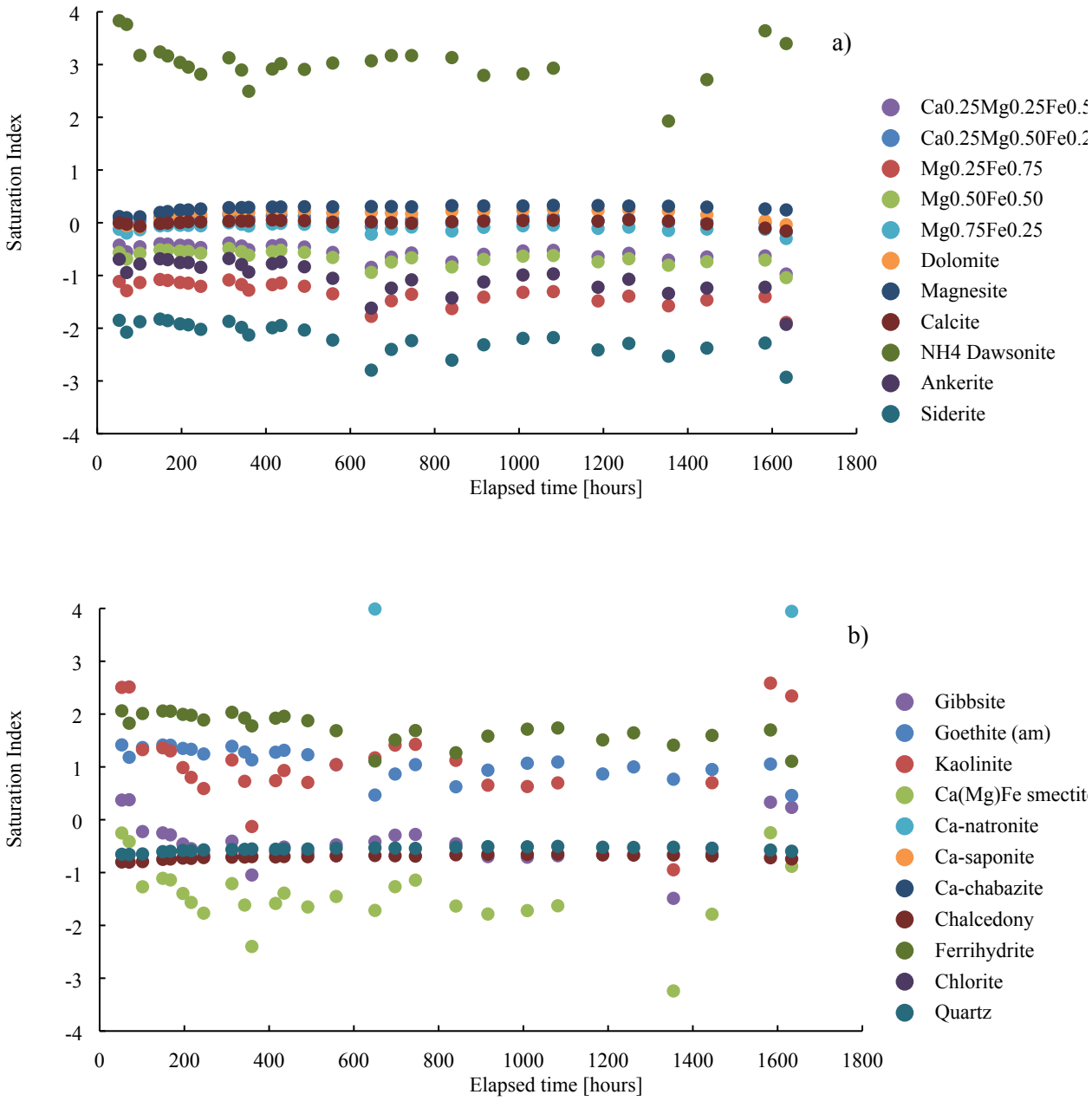

Figure 3. Saturation indices of the major (a) carbonate and (b) silicate phases of the G400 experiment (see Table 2).

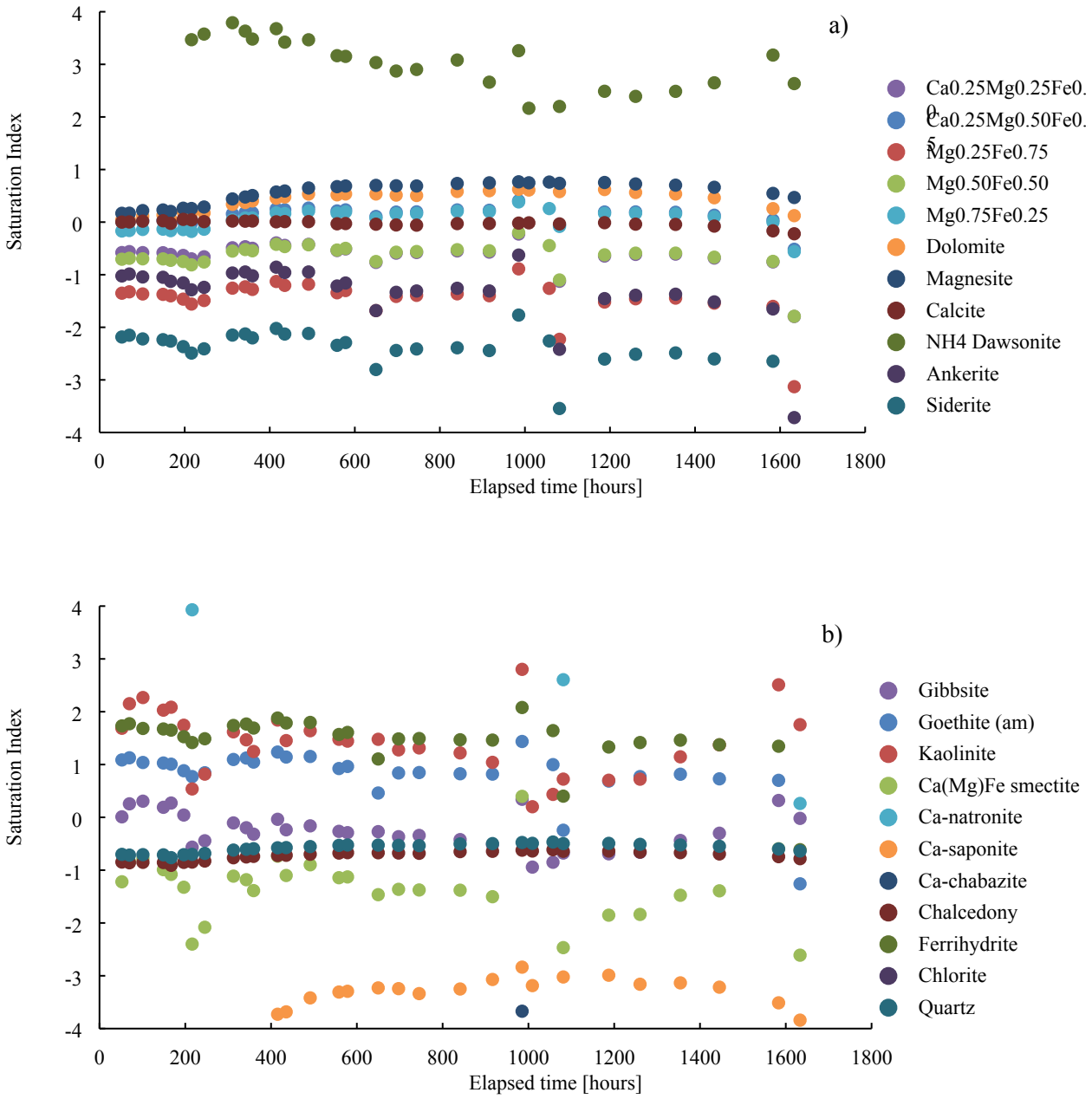

Figure 4. Saturation indices of the major (a) carbonate and (b) silicate phases of the X400 experiment (see Table 2).

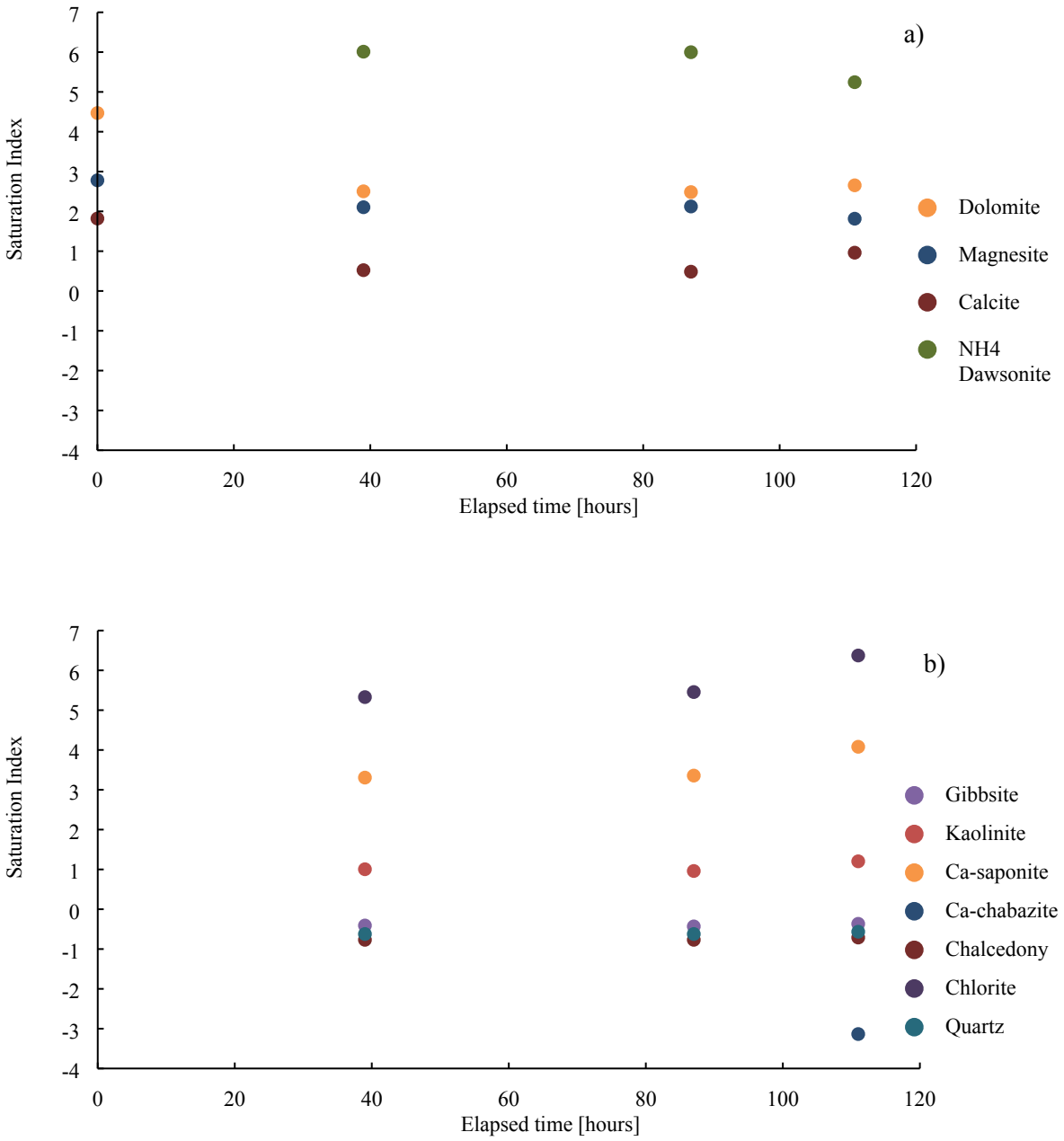

Figure 5. Saturation indices of the major (a) carbonate and (b) silicate phases of the GSW experiment (see Table 2). The iron concentration was below detection limit explaining the absence of iron bearing phases in this figure.